Florida International University
FIU Digital Commons

FIU Electronic Theses and Dissertations | University Graduate School

11-7-2012

The Nature of Microvariability in Blazar 0716+714

Gopal Bhatta
Florida International University, gopal.bhatta@fiu.edu

DOI: 10.25148/etd.FI12113013
Follow this and additional works at: https://digitalcommons.fiu.edu/etd

Recommended Citation
Bhatta, Gopal, "The Nature of Microvariability in Blazar 0716+714" (2012). *FIU Electronic Theses and Dissertations*. 761.
https://digitalcommons.fiu.edu/etd/761

This work is brought to you for free and open access by the University Graduate School at FIU Digital Commons. It has been accepted for inclusion in FIU Electronic Theses and Dissertations by an authorized administrator of FIU Digital Commons. For more information, please contact dcc@fiu.edu.

FLORIDA INTERNATIONAL UNIVERSITY

Miami, Florida

THE NATURE OF MICROVARIABILITY IN BLAZAR 0716+714

A dissertation submitted in partial fulfillment of the

requirements for the degree of

DOCTOR OF PHILOSOPHY

in

PHYSICS

by

Gopal P. Bhatta

2012

To: Dean Kenneth Furton
College of Arts and Sciences

This dissertation, written by Gopal P. Bhatta, and entitled The Nature of Microvaribility in Blazar 0716+714, having been approved in respect to style and intellectual content, is referred to you for judgement.

We have read this thesis and recommend that it be approved.

Walter Van Hamme

Caroline Simpson

Prem Chapagain

Michael Sukop

James R Webb, Major Professor

Date of Defense: November 07, 2012

The dissertation of Gopal P. Bhatta is approved.

Dean Kenneth Furton
College of Arts and Sciences

Dean Lakshmi N. Reddi
University Graduate School

Florida International University, 2012

DEDICATION

This work is dedicated to my mother Janaki Bhatta, and my father late Narayan Bhatta.

ACKNOWLEDGEMENTS

I would like to acknowledge everyone who directly or indirectly contributed to this research work. First and foremost, I am greatly indebted to my advisor, Professor James R Webb, who ushered me into the world of quasars and blazars. He was literally next door with his cheering smile - inspiring and motivating. I thank him for his patience, guidance and his confidence in me. Similarly, I thank the members of my committee for their support and advice at various stages during the writing of this dissertation. I also would like to thank the faculty, the very helpful staff and my colleagues of the FIU Physics Department for their encouragement and support that greatly enriched my years as a graduate student.

I would like to express my deepest gratitude to my mother and brother Purusottan who stood strong at the most pressing moment at home so that I could accomplish what I had already undertaken. I would like to thank my sisters Bhawani, Shanti, Dikshya, Yogamaya and Gayatri for being with the mother while I was abroad. I would like to thank my son Eshaan who had to miss me at nights while I was observing at the telescopes, and my daughter Ashlesha who arrived in the world with the completion of the work. Last but not the least, I would like to thank my wife Sukirti for always being there for me and for her unfaltering support without which this work have not been possible.

ABSTRACT OF THE DISSERTATION

THE NATURE OF MICROVARIABILITY IN BLAZAR 0716+714

by

Gopal P. Bhatta

Florida International University, 2012

Miami, Florida

Professor James R Webb, Major Professor

We organized an international campaign to observe the blazar 0716+714 in the optical band. The observations took place from February 24, 2009 to February 26, 2009. The global campaign was carried out by observers from more that sixteen countries and resulted in an extended light curve nearly seventy-eight hours long. The analysis and the modeling of this light curve form the main work of this dissertation project.

In the first part of this work, we present the time series and noise analyses of the data. The time series analysis utilizes discrete Fourier transform and wavelet analysis routines to search for periods in the light curve. We then present results of the noise analysis which is based on the idea that each microvariability curve is the realization of the same underlying stochastic noise processes in the blazar jet.

Neither reoccuring periods nor random noise can successfully explain the observed optical fluctuations. Hence in the second part, we propose and develop a new model to account for the microvariability we see in blazar 0716+714. We propose that the microvariability is due to the emission from turbulent regions in the jet that are energized by the passage of relativistic shocks. Emission from each turbulent cell forms a pulse of emission, and when convolved with other pulses, yields the observed light curve. We use the model to obtain estimates of the physical parameters of the emission regions in the jet.

TABLE OF CONTENTS

CHAPTER PAGE

LIST OF FIGURES

FIGURE PAGE

LIST OF TABLES

TABLE PAGE

CHAPTER 1

Introduction

1.1 Chapter Overview

The study of active galactic nuclei (AGN) is an important area in extra-galactic astrophysics as it involves the study of extreme gravity, high energy particles and early history of the universe. This introduction presents an overview of AGN in general. Section 1.2 describes the modern view of AGN and explores some of the major properties associated with these objects through multifrequency observations. Section 1.3 introduces blazars as a subgroup of AGN and the general classification of the objects on the basis of the luminosity, radio emission and the presence of a jet. Blazar variability is often associated with its jet, so the physical mechanisms in the jet including particle acceleration and emission processes are discussed at length. Section 1.4 focuses on the microvariability of blazars over a wide range of frequencies as observed by various research groups at various times.

1.2 Active Galactic Nuclei

Active galactic nuclei are the unresolved cores of distant galaxies that emit a tremendous amount of energy over a wide range of frequencies. The radiation emitted is highly polarized and variable over all observed time scales and at all frequencies. Some AGN are strong sources of radio emission (radio-loud quasars), and many have spectra that are characterized by broad emission lines. A modern view of an AGN proposes a supermassive black hole (SMBH) at the center, surrounded by an accretion disk that is constantly feeding the black hole with a tremendous amount of matter. In some of the radio-loud quasars, a bipolar jet emanates from the center and moves outward at relativistic speeds of $0.95c$ to $0.99c$ m s^{-1}, where c is the speed of light. The jet extends up to a few kiloparsecs (kpc) from the central engine. The central engine is enclosed in a thick cloud known as the broadline emission region (BLR) from which the broad-

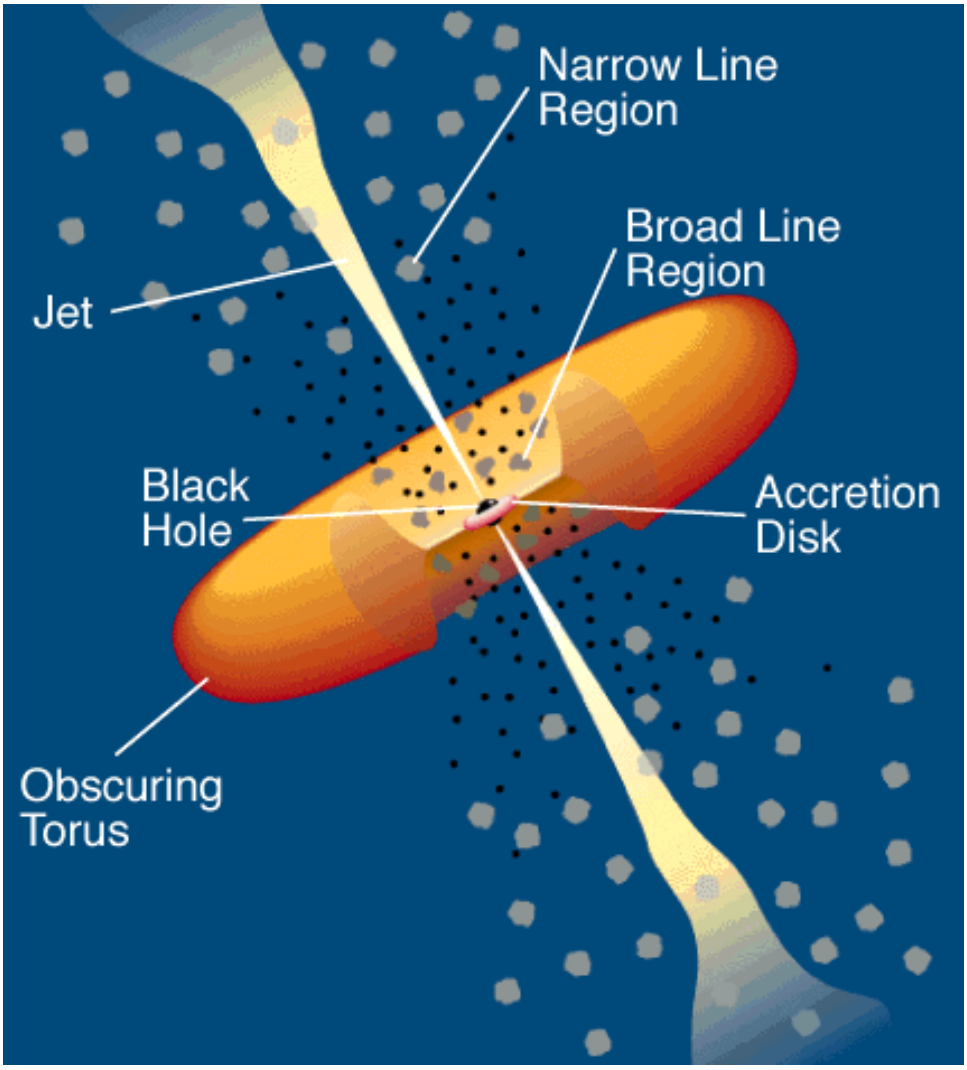

Figure 1.1: A Model due to Urry and Padovini depicting the modern concept of an AGN consisting of central engine, bipolar jet and surrounding accretion disk.

line emission in the AGN spectra emanates. A narrow line region, responsible for the narrow line emission in AGN spectra, is considered to be relatively low density clouds several kpc further away from the central engine (Krolik, 1999). Figure 1.1 shows an AGN model from Urry & Padovani (1995) depicting the location of various regions. Some of the prominent features of AGN are discussed in detail below.

AGN Properties

Most AGN viewed in the optical part of the spectrum usually appear as point sources, although for some of the relatively nearby AGN, the host galaxy can be resolved. They are often found at high redshift (> 0.1), and their angular sizes at optical frequencies are about 1 arcsec (") or less. The observed size is dependent on the wavelength. Some AGN show extended radio lobes and jets. AGN are reported to have luminosities ranging from 10^{42} to 10^{48} erg s^{-1} which is about 10^{-2} to 10^{4} times the power output of a typical galaxy. However, one also must consider that some of the AGN cores may be obscured by dust, some may be dimmer than the host galaxy, and for some the observations may be affected by relativistic beaming. This indicates that the luminosity of the AGN have a much larger range than the present data suggest. Unlike any typical galaxy, most of the AGN show broad-band power-law continuum emission from radio to γ-rays, not thermal emission which peaks as a function of temperature. The broadband continuum spectrum of 3C 279 is shown in Figure 1.2.

AGN spectra usually have strong emission lines that often show broad wings extending from a several hundred to a few thousand of km s^{-1}. Permitted and forbidden lines are both seen in these cases, but forbidden lines come only with narrow profiles. AGN with only narrow lines are usually weak from the near infrared through X-rays, as most of the output is in mid infrared.

Variability is considered one of the most important properties of AGN and is observed over all timescales and at all frequencies. However, observations indicate that the amplitude of the variations are strongly dependent on frequency. High amplitude variability is often correlated with high polarization, compact radio structure, and strong high-energy γ-ray emission. The emission could be weakly polarized by propagation through the interstellar medium. Most AGN are polarized enough that we can distinguish them from stars and galaxies. The polarization is linear and no circular polarization has been detected so far. The polarization is variable in both intensity and position angle. Although AGN were first detected by their radio emission, only about 10% of

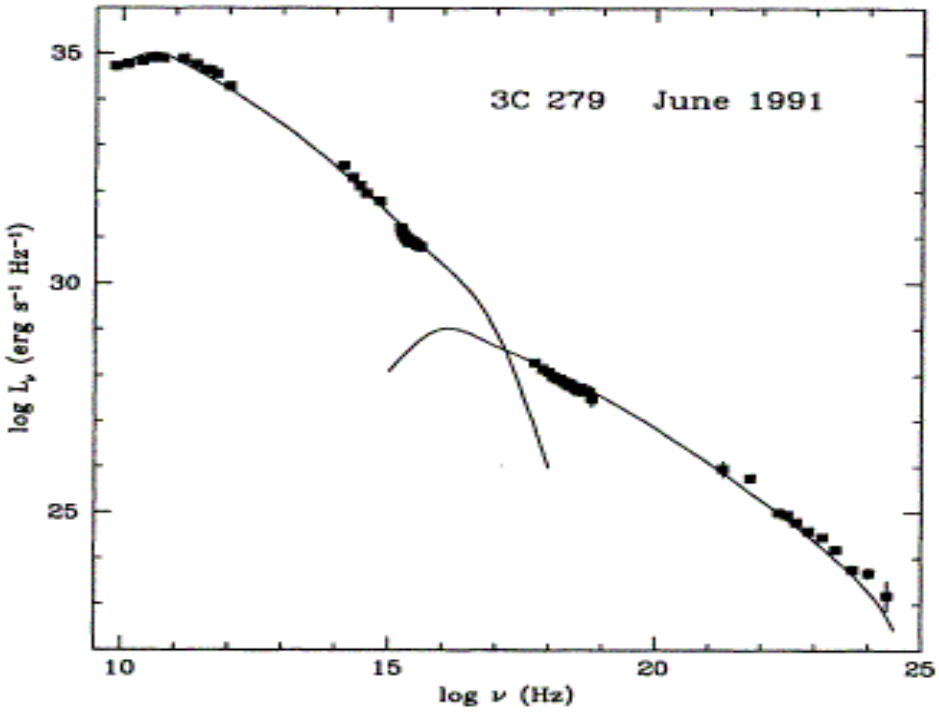

Figure 1.2: Broad band continuum emission from blazar 3C 279 (Hartmann et al., 1996)

them are radio-loud. Even those radio-loud AGN emit only a small fraction of the total power in radio. The radio-loud AGN are often associated with double-sided radio lobes in the form of relativistic jets.

AGN Classification

We do not find a universal classification of AGN. In the literature there are various classifications based on specific criteria e.g. radio luminosity, optical luminosity, γ-ray emission or the orientation of the jet. Sometimes one object may fall in two different classes due to some overlapping properties.

Seyfert galaxies are galaxies with highly luminous nuclei and a morphology similar to spiral galaxies. They exhibit strong, broad emission lines and have a blue excess and strong ultraviolet continuum. They are also counterparts of strong X-ray and infrared sources. Seyfert galaxies can be subdivided further as Seyfert type I or type II based on their emission properties. They emit strong continuum emission from the far infrared to

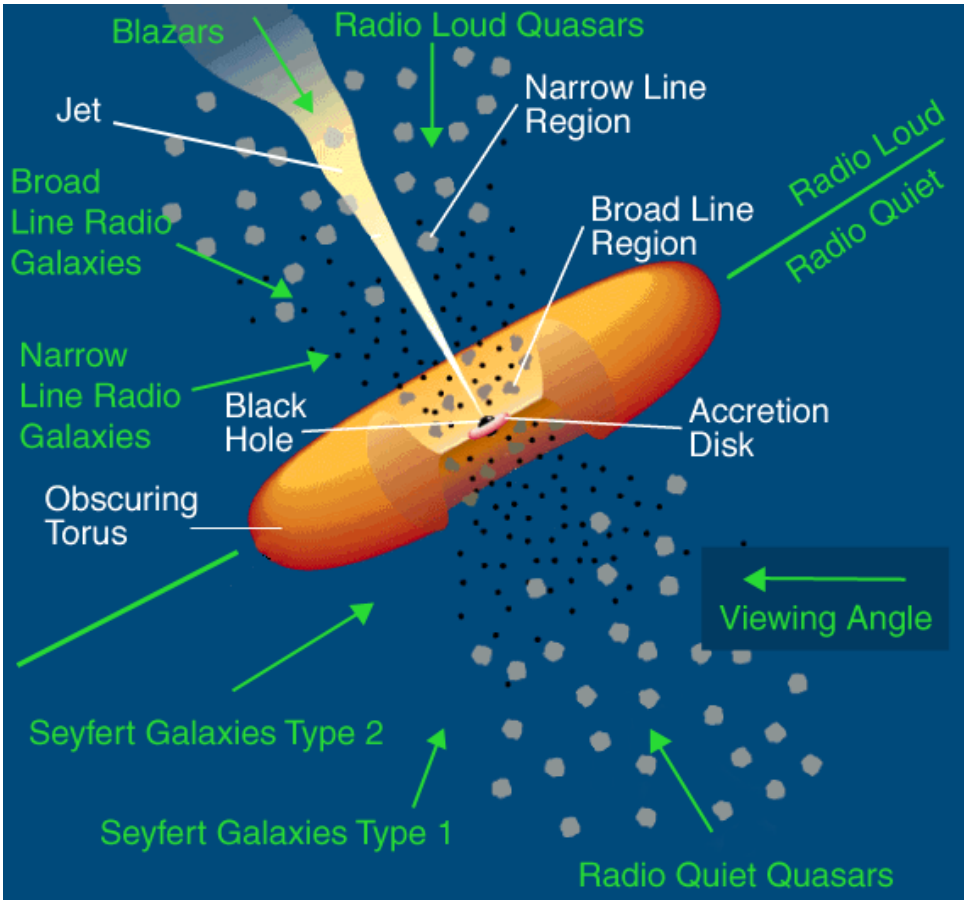

Figure 1.3: Classification of AGN based on radio content and viewing angle, as proposed by the Unified Model.

the X-ray band. They also have strong emission lines, some of which are broad, ranging from few hundred km s^{-1} to several thousand km s^{-1}. They show a weak continuum and only strong narrow emission lines.

Quasars are known to have a star-like appearance and strong emission lines. This catagory may also include the radio quiet objects which are called QSOs. The peak distribution of quasars lies at a redshift of 0.1 and these are more luminous than Seyfert galaxies. Radio galaxies are mainly elliptical galaxies with complex morphologies which emit strongly in the radio continuum. Radio galaxies can be subdivided as broad line radio galaxies (BLRG) and narrow line radio galaxies (NLRG). BL Lacertae objects (BL Lac) have strong nuclear continua that show high polarization and rapid variability. The emission lines are weak or absent. They are strong radio sources and also identified with strong X-ray emission. BL Lac objects are mainly found to be the nuclei of the

elliptical galaxies. The union group of BL Lac objects and optically violent variable (OVV) quasars are known as Blazars. They show rapid high amplitude variability. The continuum emission from blazars is mostly dominated by non-thermal emission and is thought to be beamed due to the relativistic bulk motion of the emission region towards the observer. LINERS are low-ionization narrow-emission regions. They have lower luminosity than Seyferts or quasars. They also have emission lines with low excitation. Although they are found mostly in spiral galaxies, their power source is still under debate. Some people think that the emission lines are caused by shock heating, but others believe they are excited by the same methods as the other AGN. A unified model of AGN is shown in Figure 1.3 (Urry & Padovani, 1995).

1.3 Blazars

According to the unified model of AGN, radio-loud AGN with a strong relativistic jet that is closely aligned to the line of sight are termed blazars. Blazars also refer to a subgroup of AGN that includes BL Lac objects and flat-spectrum radio quasars (FSRQ). FSRQ are characterized by some extreme properties such as high and variable polarization, rapid and high amplitude variability at all frequencies and over all time scales, high luminosity, and large beaming factors. In addition, they exhibit radio jets with individual components moving with apparent super-luminal speeds. The extreme properties of blazars are thought to be consequences of non-thermal emission from relativistic jets (Blandford & Konigl, 1995). The spectral energy distributions (SED) are in the shape of a double peaked curve. The low energy peak lies between the radio to X-ray spectral region and is considered to be from synchrotron emission produced by relativistic electrons in the jet. The higher peak in the γ-ray region is attributed to inverse-Compton emission, where the same internal photons or external photons from the BLR are upscattered by the synchrotron electrons. Based on the energy contained in each of these peaks, they can be further classified as high-frequency BL Lac objects (HBL), the ones with more energy in the high frequency peak region, and low-frequency BL Lac objects (LBL), the ones with the more energy contained in the other region.

Blazars exhibit high amplitude and rapid variability in their spectra. The high energy emission component is often violently variable(Wehrle et al., 1998; Takahashi et al., 2000). The variability time scales are often very diverse and usually range from years to a fraction of an hour. The rapid variability often takes the form of high amplitude flares which provide a unique opportunity to study the inner jet structure in addtion to the particle accelaration and radiation emission processes. The most extreme events have been recorded in γ-ray bands (Gaidos et al., 1998). Flares recorded in the GeV and optical bands in high luminosity blazars (Wehrle et al., 1998) and in the TeV and X-ray bands in low luminosity blazars Sambruna et al. (2000) appear to be correlated. These flares are most likely to be produced by the high energy ends of the distribution of radiating particles and suggest co-spatial production of high energy and low energy particles. The flares are presumably produced in shocks formed by colliding inhomogeneities which propagate down the jet with relativistic speeds (Blazejowski et al., 2000). However, present data do not allow us to exclude other possibilities, including production of flares by inhomogeneities flowing through the jets and shocked in the reconfinement regions (Komissarov & Falle, 1997), or collisions of jets with clouds (Dermer & Chiang, 1998).

In the beginning, the most viable radiation model for relativistic jets was the synchrotron self-Compton (SSC) model (Marscher & Gear, 1985; Ghisellini & Maraschi, 1989). According to this model, the smooth, polarized, and variable low energy component of blazar spectra is produced by the synchrotron mechanism, while the high energy component results from Comptonization of synchrotron radiation by the same population of electrons which produce the synchrotron component. However, this rather simple picture changed after the discovery of very high and rapidly variable MeV-GeV fluxes in many optically violent variable (OVV) and highly polarized (HP) quasars by the EGRET instrument on the Compton Gamma-Ray Observatory (CGRO). During states of high activity, fluxes were measured to exceed the synchrotron fluxes by a factor 10 or more (Montigny et al., 1995). It was quickly realized that other processes besides SSC can be more important for γ-ray production (Blandford & Levinson, 1995).

Particle Accelaration in the Blazar Jets

The study of the variable component of the emission from the blazar jet provides us with a unique opportunity to study the jet structure at the subparsec-scale. Often rapid variability and the extension of blazar spectra to GeV and TeV energies involve injection and acceleration of particles near the base of a parsec-scale jet. In this process, the kinetic and internal energy of a jet is converted into the kinetic energy of the particles and ultimately radiation. There are several models that explain how the particle acceleration takes place in the jet. One of the widely known models of production of high amplitude short term flares involves collisions of inhomogeneities moving with different velocities down the jet (Sikora, Begelman, & Rees, 1994). The inhomogeneities ejected by the central engine with different bulk Lorentz factors greater than unity and separated by a distance, start to collide after traveling down the jet. The collisions are followed by a formation of forward-reverse shock structures, with the shocked plasma enclosed between the shock fronts and moving with the bulk Lorentz factor of the contact discontinuity surface. The collisions accelerate the particles to Lorentz factors of a few thousands and produce strong non-thermal radiation. The electrons are heated to medium energies before they are accelerated relativistically by the shock waves. There are several processes which have been suggested to preheat electrons (Begelman & Sikora, 1987; Shimada & Hoshino, 2000). Marscher & Gear (1985) tried to explain an outburst as due to a shock wave passing through an adiabatic, conical, relativistic jet. They also used the model to explain the production and evolution of superluminal knots in very-long-baseline interferometry (VLBI) maps and the X-ray variability observed in 3C 273 and similar sources (Marscher & Gear, 1985). Another model used plane shock waves passing through a cylindrical jet to explain the spectral behavior observed in Mkn 521 (Kirk, Melrose, &Priest, 1994). Sikora et al. (2001) used the individual shock events in the plasma material which arise due to the velocity irregularities in the beam of the conical jet to explain the spectral behavior of X-ray and γ-ray flares. Sokolov, Marscher, & McHardy (2004) tried to simulate the multifrequency variability

seen in 3C 273 by assuming that the flares observed in it are caused by the collision of the relativistic shocks with some stationary structures such as a Mach disk.

Leptonic and Hadronic Models

The low frequency emission of the blazar spectrum is well established as being due to relativistic electrons accelerated by the passage of shock waves passing down the jet, and radiation via the synchrotron mechanism. However, the production of the very high frequency emission is not well known. There are basically two blazar models depending on the dominant γ-ray production mechanism considered: leptonic or hadronic.

The leptonic model of blazars considers an emission region which propagates with relativistic velocity along the jet. Continuous particle injection and acceleration occur at the shock front. The accelerated particles then undergo subsequent radiative and adiabatic cooling. Some of the particles possess sufficient energy to escape from the emission region and do not contribute to the emission. During this process, the kinetic energy of the jet gets converted into radiation energy and the jet decelerates (Ghisellini, Tavecchio, & Chiaberge, 2005). In this model, the high energy radiation is explained as inverse Compton scattering of the seed photons by ultrarelativistic electrons. If the seed photons are provided by the synchrotron photons in the same spatial zone, then it is known as Synchrotron Self-Compton (SSC). But if the seed photons come from an external radiation field, it is called an External Compton (EC) model. The external sources of these photons for the EC process may direct disc radiation (Dermer & Schlickeiser, 1993), broad-emission- line-region (BELR) (Sikora, Begelman, & Rees, 1994), disc radiation scattered by the gas surrounding the jet (Blandford & Levinson, 1995), or jet synchrotron radiation scattered/reprocessed back to the jet by the external gas (Ghisellini & Madau, 1996). In addition to the comptonization of the soft seed photon, the leptonic model of blazar also includes the other interactions such as γ absorption, pair production, and synchrotron self-absorption.

A hadronic model of blazars was first considered by Mannheim and Biermann (Mannheim & Biermann, 1992) to explain the high frequency peak in their spectra. This model fa-

vors the protons over the electrons as the particles responsible for the production of very high energy γ-rays as seen in the most of the blazar spectra. The protons are accelerated to ultrarelativistic energies in intense magnetic fields of at least several tens of gauss at the shock front. Protons have larger gyration radii, so they can travel a longer distance along the jet. The shocked protons acquire more energy than required to initiate pion production. Therefore, a proton-induced cascade is initiated in which protons interact with soft photons to produce pions (Mannheim, 1993). These pions consequently decay into neutrinos, electron-positron pairs and γ- rays. As the process produces high energy γ- rays, the model helps to explain the teraelectronvolt (Tev) blazar spectra.

1.4 Microvariability

Emissions from blazars that are produced predominantly through nonthermal processes vary on time scales from years to less than a day over a wide range of frequencies. Microvariability is commonly used to describe variations on time scales of about one day or less. A conversion of observed time scales into the source frame is given by $t_{source} = t_{obs}/(1 + z)$, where z is the corresponding redshift. Variability time scales have been defined in various ways, but the most common time scale is given by $t = F/(\Delta F/\Delta t)$, where ΔF is the change in the flux during the time interval Δt. With the time scales thus obtained, causality arguments can be used to limit the radius of the emitting region to $r < ct$. Hence the variations on time scales of less than a day provide constraints on the source structure on linear scales smaller than 1 AU. Although the phenomenon of microvariability in AGN is now established by various observations and analysis methods, many early reports about microvariability were received with skepticism. The rapid variability was considered as propagation-induced effects rather than instrinsic variations. Numerous factors were attributed as its cause such as instrumental instabilities (Beall, Snyder, &Wood, 1988), interstellar scintillation (ISS) and gravitational microlensing (Paczynski, 1986).

Blazars have been observed over a very wide range of frequencies, and found to have very broad energy distributions. A large fraction of the prominent radio sources includ-

ing 0716+714 and 0804+499 have been found to be also strong emitters of high-energy γ-rays with a variable component (Michelson et al., 1994). Mkn 421 was claimed to have exhibited an increase of γ-ray flux by a factor of 2.3 within 24 h at 1 TeV (Kerrick, 1995). Rapid variations of blazars have frequently been reported in the X-ray frequency region, where radio-loud and radio-weak objects have shown substantial variations on time scales shorter than one day (Snyder et al., 1980). The rapid X-ray variability of blazars has usually been described by low-amplitude fluctuations around a steady mean with occasional flares (Giommi et al., 1990). It was found that BL Lac objects such as 0716+714 and PKS 2155-304 spend only 10% of their time in spectacular flares, whereas the rest of the time they stay within a 50% range of their long-term average (Witzel & Quirrenbach, 1993; Brinkmann et al., 1994). Variations on time scales of 30 seconds were found in radio-weak source H0323+022 (Feigelson et al., 1986) and a factor of 4 increase in 4 hours was found in another radio-weak source PKS 2155-304 (Kohmura et al., 1994). Similarly, a 60% flare in 200 seconds in PKS 0558-504 (Remillard et al., 1991), and a 60% increase within 500 seconds 0716 +714 (Wagner et al., 1995) was observed. The variations in those four objects are so fast that relativistic beaming of the X-ray emission had to be invoked in order not to violate the Eddington limit Elliot & Shapiro (1974). It was shown that the extremely fast emission changes were related to the injection and acceleration of particles (Lesch & Pohl, 1992; Kirk & Mastichiadis, 1992). The variations in the flux on time scales of minutes also suggested that the X-ray emission was beamed relativistically. Changes in radio-loud sources were successfully modeled in inhomogeneous jet-models with a radial change in cut-off frequency (George, Warwick, & Bromage, 1988). The flux variability measurements in ultraviolet (UV) were also monitored and compiled Edelson (1992). The UV variability in PKS 2155-304 and OJ 287 on time scales of 1 and 2 days, respectively, were observed Maraschi et. al. (1986). Variations of PKS 2155-304 on time scales of a few hours were reported in the 1600-2600 $\mathring{A}$ band (Edelson et al., 1991) and low-amplitude variability (15%) on time scales of 0.04 days was found in the far UV at 100 $\mathring{A}$ (Marshall, Carone, & Fruscione, 1993).

Early optical monitoring of blazars on short and long term variations have been extensively reviewed (Angel & Stockman, 1980; Webb, 1988). It was found that photometric and polarimetric variations of BL Lac occurred over a period of one week, with 0.1 mag variations throughout individual and between subsequent nights (Moore et al., 1987). PKS 2155-304 showed oscillations of about 1 day (Courvoisieret al., 1995). In a four-week campaign, 0954 + 658 showed well defined, rapid and symmetric flares with exponential slopes , whereas 0716+714 exhibited oscillatory variations (Wagner et al., 1993) . Similarly, early reports of short time scale radio variability were made for BL Lac (Harvey et al., 1972), 3C 273 (Efanov et al., 1977), and OJ 287 (Bruyn, 1988). These observations established microvariability at radio frequencies as a frequent phenomenon. At radio frequency, the discovery of variations in the intensity of the emission of extragalactic objects showed that the synchrotron radiation results from a nonstationary emission process in the blazar jets (Sholomitskii, 1965), (Dent, 1965). These variations also suggested that the photon densities in the sources were so high that Compton scattering of relativistic electrons with low-energy photons emitted by them would quickly lead to catastrophic cooling, known as the inverse Compton catastrophy. Unobserved high X-ray fluxes (Hoyle, Burbidge, & Sargent, 1966) from these sources led to the suggestion of bulk relativistic motion (Shu, 1996). VLBI observations of the blazar jets in the form of radio knots proved the existence of postulated compact regions, and the apparent superluminal motion. This gave direct observational evidence for the existence of relativistic motion.

The polarization in OVV and BL Lac objects is generally found to be high ($> 3\%$). Variability of polarization in the optical domain has been found for almost all well-studied, rapidly variable blazars. Polarimetric variations in BL Lac down to time scales of a few minutes have been investigated (Moore, Schmidt, &West, 1987). The study showed that the path in the Stokes plane is generally a random walk down to time scales of 30 min. The spectral variations of the polarization and the polarization angle, as well as temporal variation of the frequency dependence of the polarization, have also been reported (Holmes et al., 1984).

1.5 Summary

Blazars are the most violent type of AGN. Their non-thermal emission is associated with a relativistic jet closely aligned to the line of sight. Variability in all timescales and over a wide range of frequencies is one of the typical characteristics of blazar emission. Variability of blazar over very short timescales of a few minutes to a few hours is termed microvariability. The study of microvariability plays a very important role in figuring out the dynamic processes in the blazar jet.

CHAPTER 2

A WEBT Campaign on Blazar 0716+714

2.1 Chapter Overview

This chapter presents the international Whole Earth Blazar Telescope (WEBT) campaign on the object 0716+714. We conceived, organized, and conducted this campaign which took place from February 22 - 25, 2009. The data obtained from the campaign form the basis of this dissertation. Section 2.2 introduces to the campaign. Section 2.3 explains the details of the observations gathered during the campaign. Section 2.4 presents the light curve obtained from the campaign with detailed data.

2.2 Introduction

Blazar S5 0716+714 (DA 237, HB 89) is located at high declination (+71^o) and is fairly bright, making it an ideal candidate for microvariability observations. Because of its featureless spectrum and its strong optical polarization, it was classified as a BL Lac object (Biermann et al., 1981). Its redshift of $z = 0.31 \pm 0.08$ was derived by optical imaging of the faint underlying galaxy (Nilsson et al., 2008). S5 0716+714 is also one of the best studied blazars since its discovery in 1979 (Kuhr et al., 1981). The blazar shows high variability over the whole electromagnetic spectrum on diverse time scales (see Wagner & Witzel, 1995; Ghisellini et al., 1997; Nesci et al., 2005; Wu et al., 2007; Zhang et al., 2008). This source has shown correlated intraday variations at optical and radio frequencies (Quirrenbach et al., 1991). Optical observations over a period of ten years indicate it experiences nearly continuous micro-variability activity with a duty cycle of about 95.3% (Webb, 2007, 2010). It is also reported as a γ-ray emitting object associated with an FR II radio component (Montagni et al., 1995; Wagner et al., 1996).

Optical microvariability studies involve the continuous monitoring of the object for an extended period of time, and follow by analyzing the time series data. Most of the optical studies are motivated by finding any kind of periodicities in the data. Such time

scales in turn may correspond to dynamical time scales such as light crossing time, rotational time scale, etc., and therefore shed light into the underlying physical processes in the blazar. Attempts to find periodicities or significant correlations for 0716+714 have been done with the extensive variability data available. Nesci et al. (2005) used long term light curves from 1953 to 2005 and reported finding evidence for long-term variability consistent with a precessing jet. Raiteri et al. (2003) reported a $\sim$ 3.3 year period in their data. Examination for periodicities in the short-term variability time frames yielded high-significance peaks at $\sim$25 and $\sim$73 minutes in twenty-two well sampled microvariability curves (Gupta, Srivastava, & Witta, 2009). Among the numerous micro-variability studies of this object in the literature, Villata et al. (2000) performed a very densely sampled WEBT observation and obtained 635 data points over 72 hours. They found that the steepest rise and the steepest decline were both roughly 0.002 magnitudes per minute over several hours, with no apparent difference between the rise and decline rates. Time series analysis of seven high time resolution micro-variability observations yielded no repeatable periodicities common in the light curves (Downs, Webb, & Pollock, 2004). Wu et al. (2005) performed nearly simultaneous multi-frequency monitoring over a span of seven days and Wu et al. (2007) used an objective prism set up to obtain truly simultaneous multicolor observations over several nights. Montagni (2006) monitored the source for micro-variability between 1996 and 2003, finding the most rapid variations were on the order of 0.1 magnitudes per hour over a period of two hours. Most slopes however were much smaller, in the 0.02 magnitudes per hour range. They also found no difference between the rise and decline rates.

The previous monitoring studies were limited in time because of the diurnal cycle for the site. In fact, this is an obviously unavoidable situation for an observer who wants to observe an object continuously for more than the length of the night. Therefore, any analysis made on a data set interrupted by the length of the day could not reveal periods longer than twelve hours. We organized an international campaign through the WEBT to observe 0716+714 over a three day period as a possible solution to the limited data

set problem. We requested observers around the world to observe S5 0716+716 during this period using standard photometric techniques, a common set of comparison stars, and in a common filter.

2.3 The WEBT Campaign and Observations

WEBT observers carried out the planned three days of intensive micro-variability observations of 0716+716 from February 22, 2009 to February 25, 2009. We selected a February observation date when 0716+716 would be readily accessible the entire night from most sites. Thirty-six observatories in sixteen countries around the world participated in this continuous monitoring program and submitted data for compilation into a continuous light curve and subsequent analysis.

The response to the call for observers through WEBT was excellent and plans were made to carry out the observations. The primary observing band was chosen to be the standard Johnsons & Cousins R since most observatories regularly use the filter for micro-variability observations. We divided the observatories according to longitude regions to help coordinate the observations. It was also decided that if there were multiple telescopes in each longitude range, then at least one telescope would be assigned a different filter so as to obtain simultaneous color information as the observation progressed. However, the continuity of the R light curve was the highest priority in this campaign.

To achieve a consistent differential photometry throughout the campaign, not only we used a common filter system but also a common set of four comparison stars from the sequence of Villata et al. (1998) shown in Figure 2.2. As stars 1 and 2 are usually overexposed in brightness, we chose to use only stars 3, 4, and 5 as comparison stars and calculated the magnitude of star 6 as a check star. The latter step would make sure that the magnitude obtained for the object from the differential photometry is accurate and consistent for all the observers. Table 2.1 lists the longitude zone, a code assigned to each observatory, the country, the observatory name, the longitude, telescope size and the filters used.

Zone	Code	Country	Observatory	Longitude (degree)	Telescope (m)	Filters
1	AAS	Spain	Agrupacion Obs.	0.73	0.50	R
1	AVO	Italy	Aosta Valley Obs.	7.36	0.81	RI
1	MAO	Germany	Michael Adrian Obs.	8.41	1.20	BVRI
2	AAO	Italy	Armenzano Obs.	12.69	0.36	R
3	TUR	Finland	Tuorla Observatory	22.17	0.35, 1.0	R
3	BEL	Bulgaria	Belogradchik	22.60	0.60	BVRI
3	HANK	Finland	Hankasalmi	26.50	0.40	BVRI
3	STPET	Russia	St. Petersburg	29.82	0.40	R
3	JAKO	Finland	Jakokoski Obser	30.00	0.50	I R
4	CRIM	Crimea	Crimean AP Obser.	30.20	2.6, 1.25	R
5	ABAS	Georgia	Abastumani Obs.	42.80	0.70	R
6	ARIES	India	ARIES	71.68	1.04	R
7	BAO	China	BAO, Xinglong	114.00	1.00	R
8	WHO	China	Weihai China	122.00	1.00	BVRI
8	LOAO	USA	Mt. Lemmon	249.00	1.00	R
11	MDM	USA	MDM Kitt Peak	249.00	1.30	R
11	SARA	USA	SARA/Kitt Peak	249.00	1.0	R
12	BUO	USA	Butler	273.55	0.96	R
12	DSO	USA	Dark Sky Obs.	278.58	0.60	R
13	BLK	Ireland	Cork	352.00	0.40	RGB

Table 2.1: Observatories contributing observations to the WEBT campaign

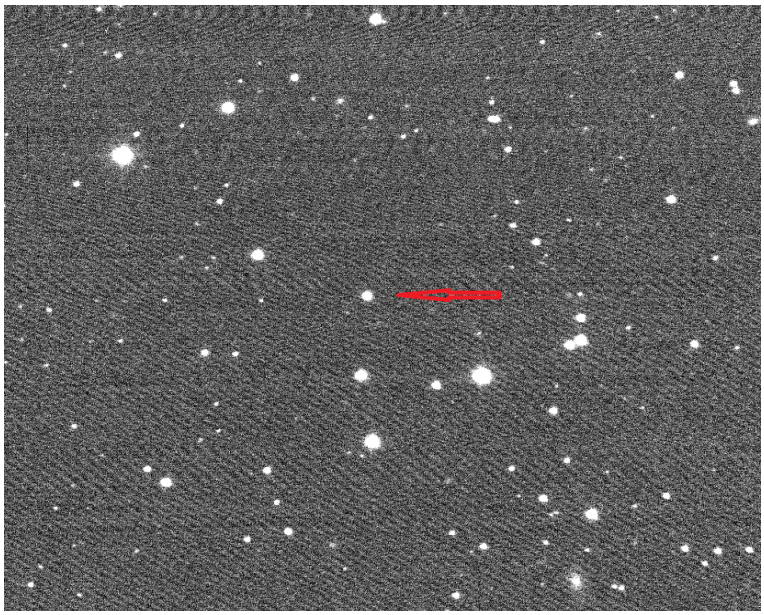

Figure 2.1: A typical CCD image of blazar 0716+714 observed from SARA, Kitt Peak 0.9m telescope

0716+714 (S5 0716+714)

Coordinates
α = 07:21:53.447 δ = +71:20:36.35 (2000)
z = 0.3 (?)

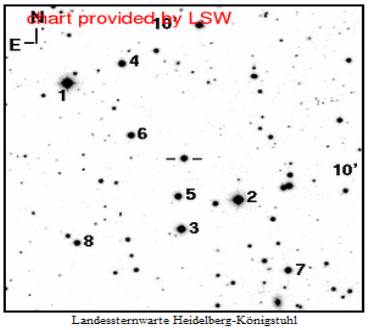

Landessternwarte Heidelberg-Königstuhl

Comparison stars

star	U	B	V	R	I	J (1.24 microns)	H (1.66 microns)	K_s (2.16micron)
1		11.54(0.01)	10.99(0.02)	10.63(0.01)		10.050(0.018)	9.813(0.017)	9.750(0.020)
2		12.02 (0.01)	11.46 (0.01)	11.12 (0.01)	10.92 (0.04)	10.515 (0.021)	10.301 (0.017)	10.228 (0.020)
3		13.04(0.01)	12.43(0.02)	12.06(0.01)	11.79 (0.05)	11.319 (0.020)	11.063 (0.017)	10.978 (0.022)
4		13.66(0.01)	13.19(0.02)	12.89(0.01)		12.275 (0.023)	12.045 (0.021)	12.039 (0.025)
5		14.15(0.01)	13.55(0.02)	13.18(0.01)	12.85 (0.05)	12.341 (0.021)	12.066 (0.019)	12.010 (0.026)
6		14.24(0.01)	13.63(0.02)	13.26(0.01)	12.97 (0.04)	12.479 (0.023)	12.212 (0.021)	12.166 (0.027)
7		14.55(0.01)	13.74(0.02)	13.32(0.01)		12.453 (0.021)	12.071 (0.021)	12.006 (0.025)
8		14.70(0.01)	14.10(0.02)	13.79(0.02)		13.072 (0.021)	12.778 (0.025)	12.736 (0.034)

comparison stars from Villata et al., 1998, A&AS 130, 305
I-data from Ghisellini G. et al., 1997, A&A 327, 61
JHK-data from 2MASS

Field of view is 10'x10'

Figure 2.2: Blazar Finder Chart for the blazar from Villate et al. (1998)

Most of the observers sent the data in the form of magnitudes of the blazar along with other information including the exposure times of the images and magnitude errors. Table 2.2 presents the details of the campaign data submitted by each of the observers. column 1 is the name of the participating observatory, column 2 is the time in Julian Date during which the images were taken, column 3 is the number of data points, column 4 is the filter of the telescope, column 5 is the exposure time of the images as sent by the observers, and column 6 is the mean instrumental error in the magnitudes as reported by the observer. The mean error of the whole campaign is 0.010 magnitudes. The data contributed by the FIU group for the campaign were obtained with the 0.9 m telescope in Kitt Peak Arizona. The images were taken by James Webb and Gopal Bhatta using a charge coupled device (CCD) camera on February 24, 25 and 26. The images on the 25th showed a large scatter due to passing clouds in Arizona. The images then were reduced using the software Miramatrics (MIRA) and the magnitudes were obtained by the photometry package in the software.

Observatory	JD-2454800.000 (day)	Npts	Filter	Exp. Time (s)	Mean Err. (mag)
Abustumani	86.163-86.488	240	R	NA	0.007
	87.222-87.447	46	R	NA	0.006
	89.169-89.449	178	R	NA	0.008
Agrupacion	88.262-88.378	90	R	NA	NA
ARIES	88.612-88.852	159	R	NA	0.003
Armenzano	86.308-86.360	115	R	NA	NA
Astoa Valley	86.286-88.562	97	R	240	0.005
Belogradchick	87.226-87.474	6	R	NA	NA
	87.224-87.473	6	V	NA	NA
	87.227-88.489	371	I	NA	0.007
DSO	86.504-86.882	700	R	NA	NA
Guadarrama	86.321-86.366	59	R	30	0.066
Hankasalmi	88.191-88.536	270	R	60	NA
Jakokoski	88.383-88.584	106	IR	120	0.008
LOAO	87.227-88.489	371	I	NA	0.007
	86.618-87.003	411	R	NA	NA
	87.737-88.017	218	R	NA	NA
	88.594-89.015	667	R	NA	NA
Michael Adrian	87.413-873671	119	V	NA	0.002
NAO	87.054-87.237	62	R	60	0.007
	88.005-8.219	185	R	60	0.008
	89.123-89.213	100	R	60	0.010
Pulkovo	88.174-88.651	209	R	NA	0.014
SARA	86.660-86.835	579	R	20	0.002
	87.745-87.769	43	R	20	0.001
	88.654-88.954	791	R	20	0.001
Tuorla	87.365-88.420	138	R	NA	0.016
WHO	88.203-88.303	33	R	102	NA
	89.229-89.298	69	R	40	NA
	89.963-90.040	78	R	60	NA

Table 2.2: Details of the data acquired during the WEBT campaign

2.4 The Light Curve

Figure 2.3 presents the long continuous optical micro-variability light curve of 0716+714 obtained during the multi-site observing campaign. The Blazar showed continuous variability over a 0.5 magnitude range. The observations covered the time period between JD 2454886.1 (2/23/2009) and JD 2454889.5 (2/26/2009). There was nearly continuous coverage between Julian date (JD) 2454887.3 and 2454888, with overlap from several observatories during many time intervals. The data were reduced on-site and sent to the collaboration as magnitude files. The magnitudes were then combined, noting where overlaps occurred, and examined for possible offsets due to CCD-filter combinations. The data from each observer are plotted in a different color in Figure 2.3. with codes given in Table 2.2. Inspection and overlaying the observations revealed some offsets due to instrumental/filter differences, but most of the data were of sufficient quality and had sufficient overlap so minor zero-point adjustments could be made to correct for these instrumental differences and to obtain a consistent continuous light curve. In all cases, the data with the lowest noise and that had the best overlap with other data sets were used to determine the offsets for the other light curves. Exposure times for individual images ranged from 30 seconds to 120 seconds depending on the observatory and telescope. The amplitude of the variability A, is 39.31%, as given by Heidt & Wagner (1996)

$$A = 100 \times \sqrt{(A_{max} - A_{min})^2 - 2\sigma^2},\ \% \tag{2.1}$$

where A_{max} and A_{min} denote the maximum and minimum magnitudes of the blazar in the light curve, and σ the variance.

The campaign statistics are presented in Table 2.3. Only 2613 of the highest quality data points were included to construct the final light curve, although the total number of data points acquired for the whole campaign is about 4350. The mean magnitude of the blazar during the campaign was found to be 13.75 with a standard deviation of 0.098. The highest fluctuation recorded was 0.31 magnitudes which is nearly 30% change in

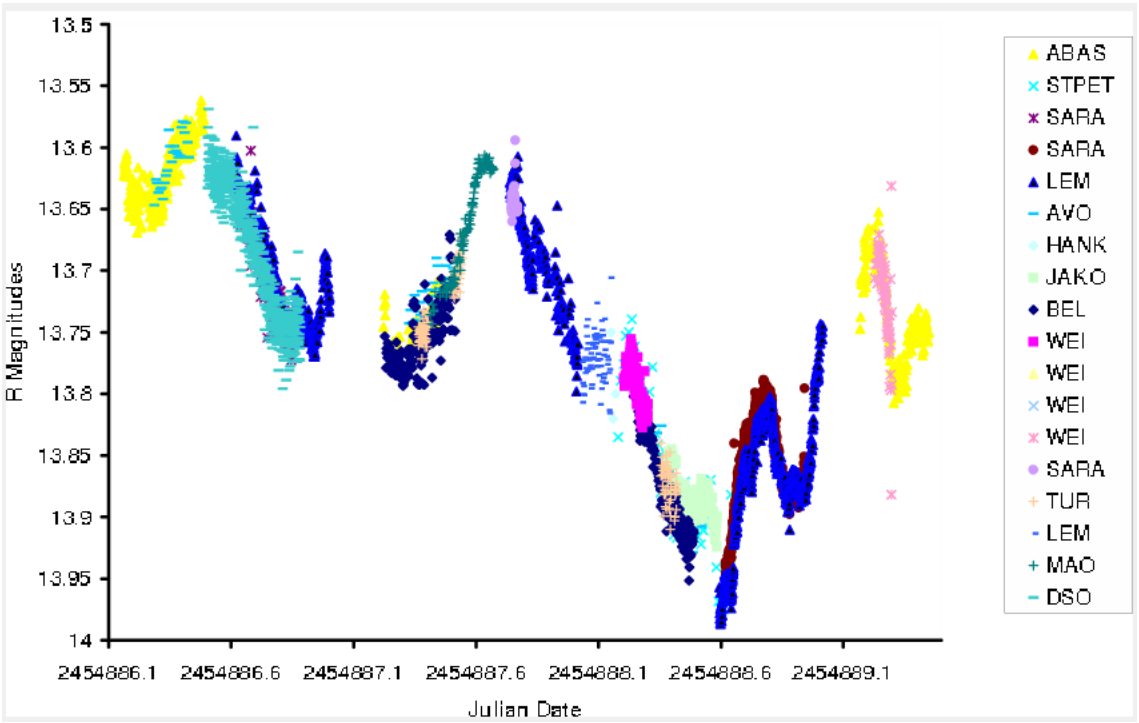

Figure 2.3: The raw light curve of S5 0716+714. Each data set contributed is plotted with different symbols and identified according to the codes given in Table 1.

Time length of the Campaign	78.88 hrs
Number of the data points	2613
Mean Magnitude(R)	13.75
Maximum Magnitude (R)	13.962
Minimim Magnitude (R)	13.571
Largest Oscilllation	0.311 (mag)
Standard Deviation	0.098 (mag)

Table 2.3: Campaign Statistics

flux.

The RMS scatter for each data set was calculated and the data were then plotted together for each segment of the light curve. The data were smoothed using the criterion that for any data point $x_i > (x_{i+1} + x_{i-1})/2 + 0.005$, then $x_i = (x_{i+1} + x_{i-1})/2$. This criterion was based on the assumption that in a time period as short as two minutes, a data point can not be too different from the average of the previous and the following data points. The magnitudes were converted to flux using standard flux conversions for the R filter, a redshift of 0.30, and Galactic absorption of 0.031 magnitudes. Figure 2.4 shows the complete smoothed flux curve. It can be seen by comparing figures 2.3 and 2.4 that the smoothing keeps the major trend of variation unchanged. The total length of the smoothed light curve was 3.28 days.

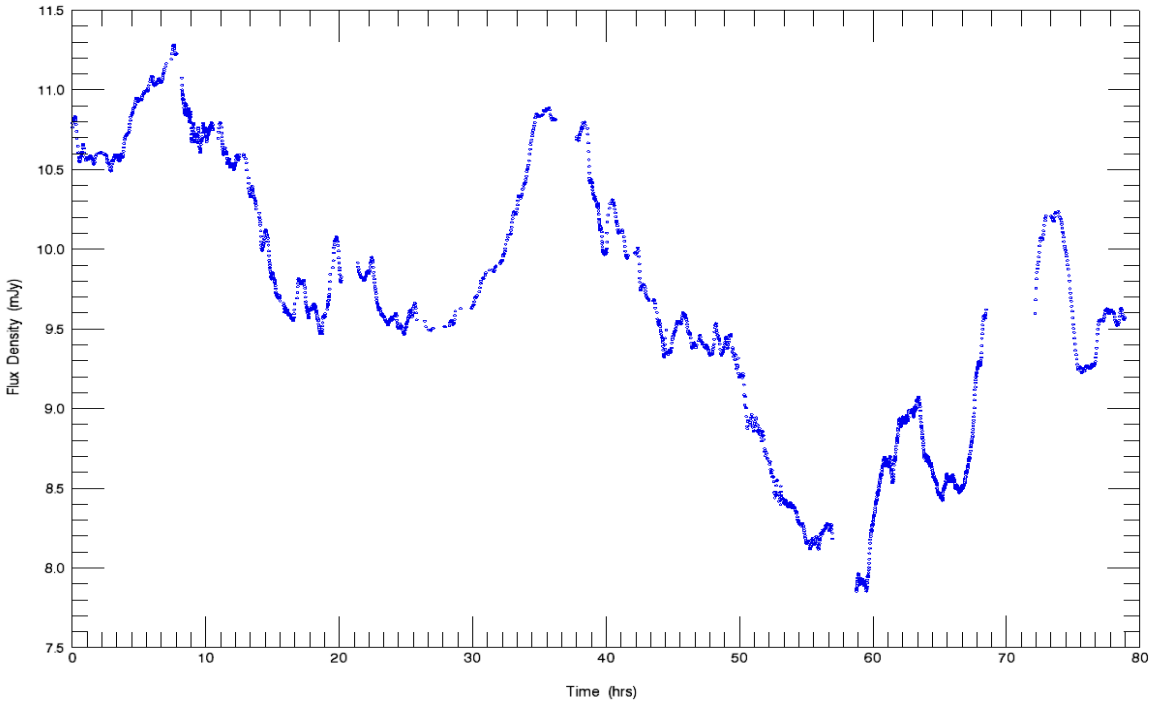

Figure 2.4: The smoothed light curve of 0716+71 using the algorithm discussed in the text.

We analyzed individual segments of the smoothed light curve to determine the maximum rise and decline rates seen during the observation. Twelve individual rapid excursions were noted in the light curve. We fit a linear model to each of those segments to determine the maximum climb and decline rates, concentrating on only segments

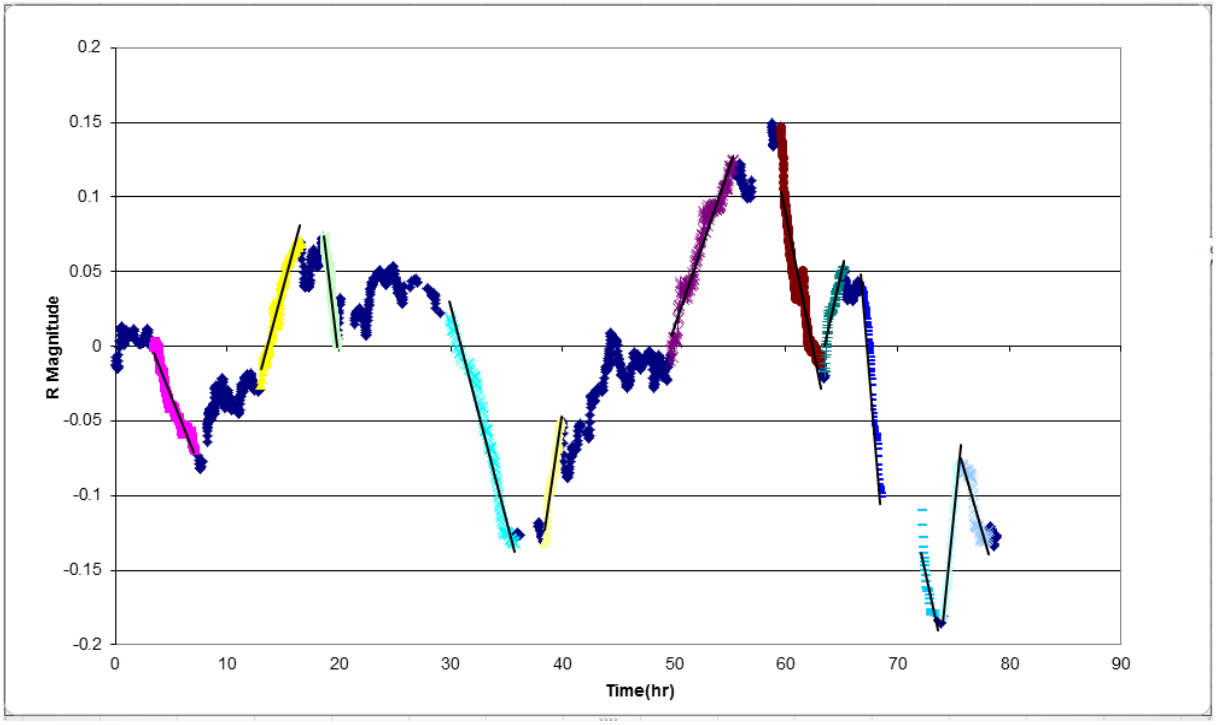

Figure 2.5: The slopes of twelve sections of the light curve .

which had a large number of data points. Table 2.4 lists the slopes and correlation coefficients for each of the segments we examined. The first column lists the time interval of individual structure in the light curve where the slope became maximum in the neighborhood. The values of the slopes are listed in the column 2. The correlation coefficients of the linear rise or decline for each section of the light curve are presented in the column 3. Column 4 gives the number of data points included in the slope and column 5 lists whether the slope is rising or declining. The fastest rate was an increase of 0.089 magnitude per hour over a range of 0.15 magnitudes. The Pearson's correlation coefficient for that fit was R = 0.997 and it contained 99 data points. The average decline rate was 0.042 magnitudes/hour (standard deviation of 0.022) while the average rise rate was 0.043 with a standard deviation of 0.028. Thus overall, the rise and decline rates are similar to one another in this segment of light curve. These results are consistent with the maximum rise and decline rates found by other observers, (see Villata et al. (2000) , Montagni (2006)).

SN	Time (hr)	Slope (mag/hr)	Corr. Coeff.	Data Pts.	Rise/Decline
1	3.38-7.01	0.019	0.918	123	Rise
2	13.03-16.54	0.027	0.946	155	Decline
3	18.69-19.84	0.064	0.967	40	Rise
4	29.91-35.76	0.029	0.968	120	Rise
5	38.39-39.91	0.050	0.945	77	Decline
6	49.70-55.30	0.022	0.956	177	Decline
7	58.52-63.10	0.037	0.878	244	Rise
8	63.48-65.20	0.033	0.904	115	Decline
9	66.74-68.46	0.089	0.977	99	Rise
10	72.14-73.60	0.035	0.739	29	Rise
11	74.07-75.63	0.076	0.977	43	Decline
12	75.66-78.17	0.026	0.873	73	Rise

Table 2.4: Maximum slopes from light curve

2.5 Summary

The WEBT international collaboration was successful in obtaining a nearly continous light curve of 0716+714 spanning 72 hours. Although the observations were made from different sites around the globe, standard stars in the field. The standard magnitudes of the non-variable check stars in the field were used to standardize the photometric calibration. The lightcurve showed constant microvariability going through oscillations with amplitude of 39.13%. The overlap seen in the various locations of the light curve confirms that the oscillations are not instrumental in nature. The fastest rise and the fastest decline were 0.089 magnitude/hour and 0.019 mag/hour, respectively and the average rise and decline were 0.043 magnitude/hour and 0.042 magnitude/hour, respectively.

CHAPTER 3

Data Analyses

3.1 Chapter Overview

This chapter mainly focuses on the various methods used to analyze the data obtained from the WEBT campaign. Section 3.2 discusses the time series analysis of the data in the form of discrete Fourier and wavelet analyses, and discusses the conclusions from these analyses. Section 3.3 describes the noise analysis of the data to see if it is from noise processes, particularly multiplicative or lognormal noise processes. The analysis leads to a model where microvariability can be better represented as the result of emission due to additive shot pulse processes rather than random noise processes.

3.2 Time Series Analysis

Any variable which is measured sequentially in time forms a time series. In astronomy, light curves are excellent examples of a time series. Time series can be studied using various tools of Time Series Analysis. Time series analysis of a light curve looks for structures, trends, periods, or seasonal variations which are contained in the time series. There are various time series analysis techniques which are widely used in science. Some of the popular tools are Fourier analysis, wavelet analysis, structure functions and periodograms. Finding periods or structures present in data in turn provides an insight into the physical processes which cause the fluctuations. The smoothed light curve described in chapter 2 was analyzed using time series anaysis in an attempt to search for any possible periods present in the data. For the analysis, we used both Discrete Fourier Transform (DFT) and Wavelet Analysis (WA) to search for periodicities. These analyses and their results are discussed in the following sections.

Fourier Analysis

The Fourier transform is a common mathematical tool used in physics and engineering. It can be defined as the reversible, linear transformation of a time-domain signal into a corresponding frequency-domain signal (Bracewell, 1965). Mathematically,

$$f(\omega) = \int_{-\infty}^{\infty} f(t)\, e^{-i\omega t} dt, \tag{3.1}$$

is known as the forward tranform, and

$$f(t) = \int_{-\infty}^{\infty} f(\omega)\, e^{i\omega t} d\omega \tag{3.2}$$

gives the inverse transform with ωt being dimensionless.

Although the above equations define a Fourier transform, they can be used only for continuous variables. In astronomical observations, a light curve is always presented in the form of discretely sampled data points which can be evenly or unevenly spaced in time. In such cases, we use a discrete Fourier transform. For a discrete evenly sampled time series of N data points x_j, the DFT is given as

$$X_k = \sum_{j=0}^{N-1} x_j e^{-2\pi i j k/N}, \tag{3.3}$$

and the inverse discrete Fourier transform is given by

$$x_j = \frac{1}{N} \sum_{j=0}^{N} X_k e^{2\pi i j k/N}. \tag{3.4}$$

The power of the FT is given by $P = |f(\omega)|^2 = f^*(\omega) f(\omega)$, $f^*(\omega)$ being the complex conjugate. The spatial frequency corresponding to the maximum power gives the estimate for the period present in the data.

We performed Fourier transform analysis on the entire smoothed light curve. First a linear slope of -2.5×10^{-5} and a Y-intercept of 0.01 were removed to linearize the data. The resulting data then were analyzed using a DFT analysis (Deeming, 1975).

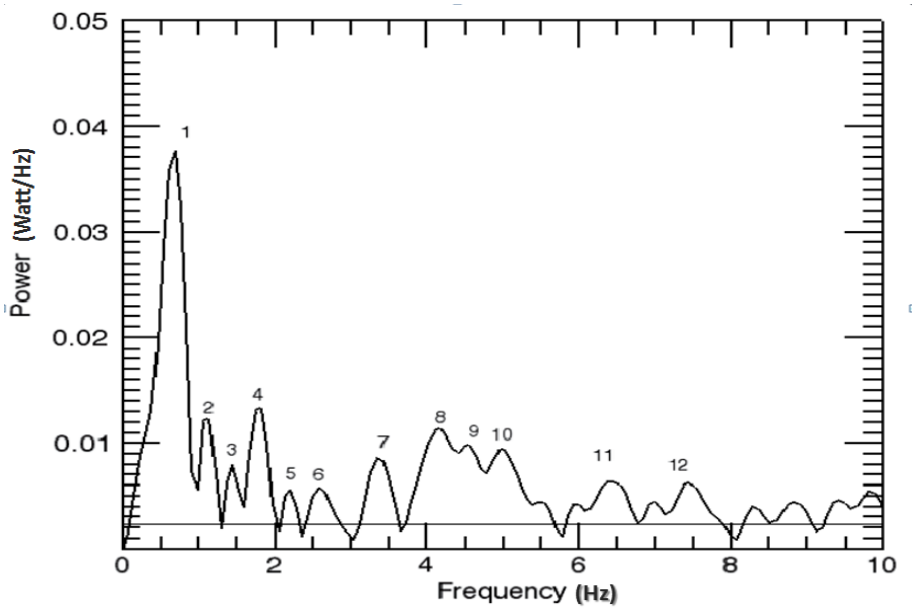

Figure 3.1: The power spectrum of the smoothed light curve. The horizontal line across the bottom indicates the maximum power level of simulated light curves with random noise of the same amplitude as the 0716+714 light curve. The numbers associated with the peaks in the power spectrum corresponds to the frequencies and periods listed in Table 3.1

The results of the unequal interval FT showed that the first significant peak represented a period of 1.46 days (35.04 hours), while a second peak occurred at 0.55 days (13.2 hours). A third peak at 0.88 days (21.12 hours) was also well above the noise level. The DFT of the light curve is shown in Figure 3.1 and all the time scales in the observer's frame resulting from it are listed in fourth column of Table 3.1. The fifth column gives the corresponding time scale in the rest frame of the blazar which is given by

$$t_{rest} = \frac{z}{\gamma\,(1 - \beta cos\theta)} t_{observed}, \tag{3.5}$$

where z, γ and θ are the red shift, the bulk Lorentz factor, and the angle of jet orientation, respectively. The values used for these parameters are described in section 4.5 of chapter 4. The line parallel to the horizontal axis near the bottom Figure 3.1 shows the DFT of the average of 100 light curves modeled in Interactive Data Language (IDL) by assuming Gaussian distributed noise a sigma (standard deviation) equal to the sigma of the data. By comparing the peaks with the line we see that they are many sigmas above

Number	Frequency (/day)	Power	Timescale (obs. frame)	Timescale (rest frame)
1	0.60	0.038	1.46 days	23.94 days
2	1.14	0.012	0.88 days	14.43 days
3	1.18	0.008	0.55 days	9.02 days
4	1.50	0.012	0.66 days	10.82 days
5	2.25	0.005	10.60 hours	173.84 hours
6	2.60	0.005	9.20 hours	155.88 hours
7	3.40	0.008	7.20 hours	118.08 hours
8	4.20	0.012	5.76 hours	94.46 hours
9	4.54	0.009	5.28 hours	85.93 hours
10	5.00	0.009	4.80 hours	78.72 hours
11	6.50	0.007	3.67 hours	60.18 hours
12	7.50	0.007	3.19 hours	52.31 hours

Table 3.1: The various periods in the light curve detected with DFT Analysis

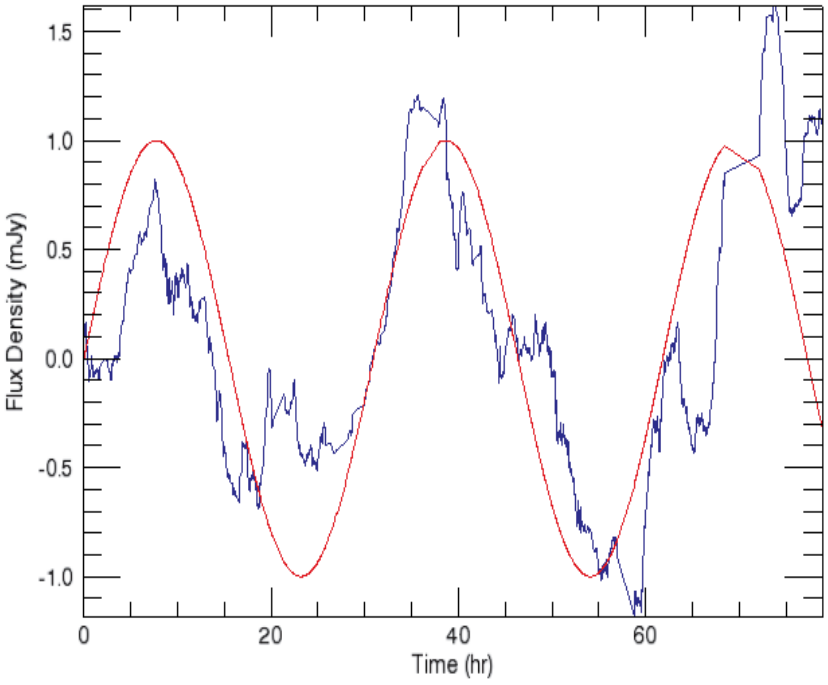

Figure 3.2: Sine curve fitted to the smoothed data with the period 1.4 days, amplitude 1.0 and phase 0 obtained from the DFT analysis. Pearson's correlation coefficient is 0.66

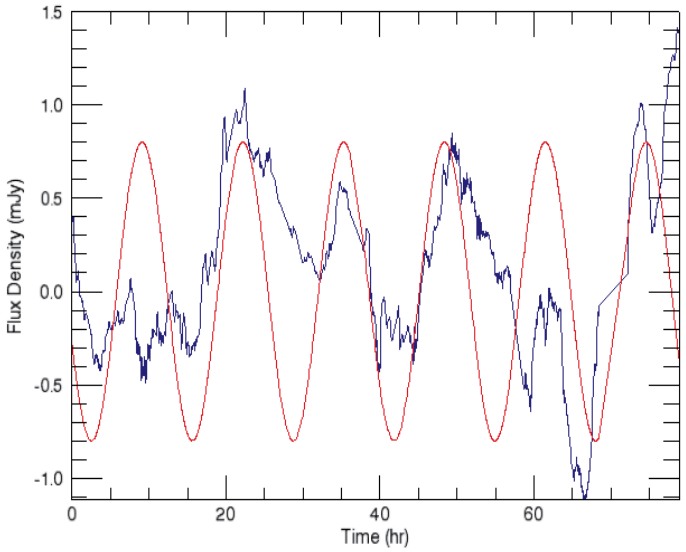

Figure 3.3: Sine curve fitted to the smoothed data with the first peak removed with a period 0.54 days, amplitude 0.8 and phase 3.4 obtained from the DFT analysis. Pearson's correlation coefficient is 0.31

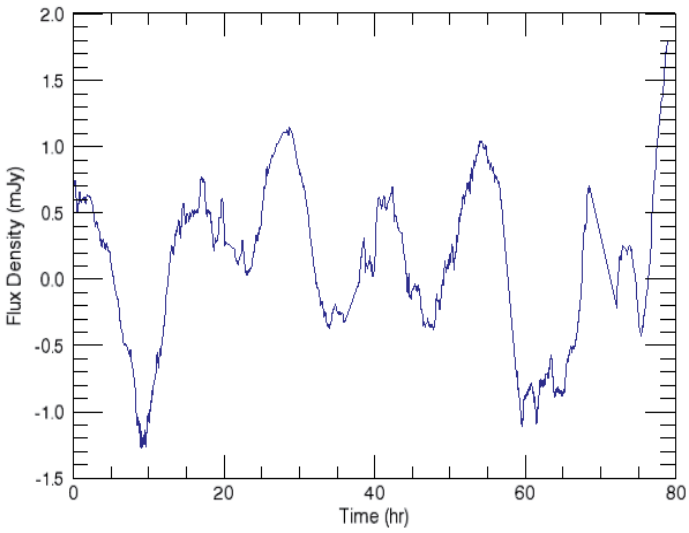

Figure 3.4: The smoothed data after two sine components have been removed. The residual amplitide increased to 1.7. For any periodic data this would decrease with successive prewhitening.

the noise level. Figure 3.2 shows in red the sinusoidal curve fit to the data with the frequency from the first prominent period obtained from DFT. We then pre-whitened the flux curve by subtracting the derived periods, adjusting the amplitude and phase for best fit as shown in Figure 3.3, and then reanalyzed the prewhitened light curve. The amplitude of the residuals seen in Figure 3.4 did not decrease drastically as we pre-whitened the data, indicating that the periods are not indicative of a true period running through the extended data set as shown in Figure 3.4. Since we failed to detect the significant periods at approximately 25 and 73 minutes seen by Gupta, Srivastava & Witta (Gupta, Srivastava, & Witta, 2009), we could not confirm any of the previously detected periods seen in 0716+714 micro-variability curves or propose significant new periods present in the long micro-variability curve. We attribute the seemingly significant peaks seen in the power spectrum to particular features in the light curve, not necessarily cyclical oscillations.

Wavelet Analysis

In spite of the fact that Fourier transform analysis is one of the most powerful tools for periodicity searches, it does not give good results for a non-stationary time series. Wavelet transform can be used to analyze time series that contain nonstationary power at various frequencies (Daubechies, 1992). A wavelet is a function with zero average that is defined over a limited domain. Thus a wavelet basis is a localized function in contrast to the sines and cosines of the Fourier series. Wavelet analysis therefore allows for localized features in time, frequency, or shape. The basic idea underlying the use of wavelets is to analyze data according to a scale or resolution. A continuous wavelet transform is given by

$$\Psi_f^{\psi}(\tau, s) = \frac{1}{\sqrt{|s|}} \int f(t)\, \psi^* \left(\frac{t-\tau}{s} \right) dt, \tag{3.6}$$

where s is the scale factor and τ is the center. Here $\psi(t)$ is the wavelet function. One of

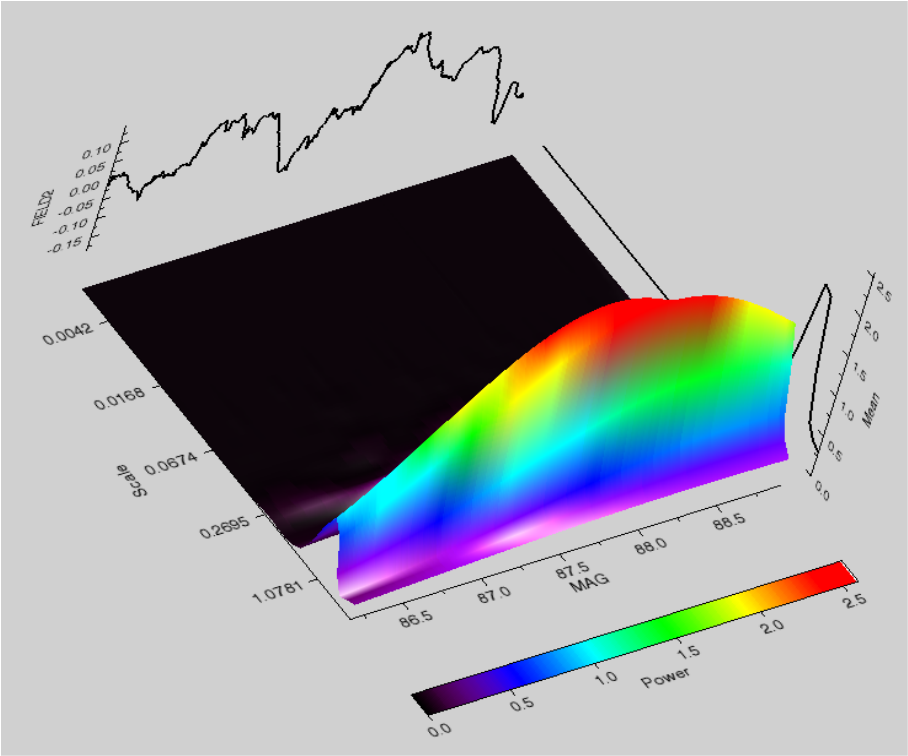

Figure 3.5: The Morlet Wavelet transform of the smoothed light curve.

the widely used wavelet functions is the Morlet's wavelet function given by

$$\psi(t) = e^{iat} e^{\frac{-t^2}{2\sigma}}, \tag{3.7}$$

where a is the modulating parameter known as the order of the wavelet and σ is the scaling parameter. A Morlet's function is a sine wave convolved with a Gaussian and its order is chosen to satisfy the admissibility condition (Farge, 1992).

We also used the wavelet application in IDL to compute the wavelet transform of the identical data set to directly compare with the DFT results. We used the Morlet kernel of order 6. Figure 3.5 shows the wavelet transform of the light curve of 0716+714. The peak of the wavelet transform corresponds with a sinusoidal oscillation with a period of 1.28 days (30.72 hours), but is clearly only significant in the central region of the data run (shown in red in Figure 3.5). It fits extremely poorly at the start of the light curve. We conclude that the results of the DFT and wavelet analysis are inconclusive at best.

3.3 Noise Analysis

Power spectrum density (PSD) is one of the useful quantities of time series analysis that characterizes the variability process. It is given by the product of the Fourier transform of the light curve and its complex conjugate. The PSD of the blazar emissions is usually parameterized as a power law,

$$P(\nu) = \nu^{-\alpha}. \tag{3.8}$$

In log-log space, α represents the slope of the PSD and for blazar emission, α is usually found to be between 1 and 2. In such cases, the PSDs reveal the red-noise character of the underlying processes which result in larger variations on the longer time scales.

Dhalla et al. (2010) used the analysis method of Vaughan et al. (2003) to examine 21 single-night micro-variability light curves of 0716+71. This analysis consists of dividing the light curve into individual bins and calculating the RMS deviation within each bin using the equation

$$x_{rms} = \sqrt{\frac{1}{N}\sum_{i=1}^{N}(x_i - \bar{x})^2}. \tag{3.9}$$

According to Vaughan et al. (2003), if light curves are stochastic, individual details will provide little physical information. However, we can consider each light curve to be one realization of the same underlying stochastic process. If the process is a stationary noise process, the realizations should exhibit similar statistical properties, e.g. a linear relationship between excess RMS and time and a Gaussian distribution of flux values. Dhalla et al. (2010) found no significant relationship between RMS and flux and the flux distribution was not obviously Gaussian. They generated 100 light curves of Gaussian noise and sampled them similarly to the individual microvariability curves. The results indicated that the current microvariability curve realizations were too short to recover the noise characteristics of the simulated light curve. This indicated that the individual

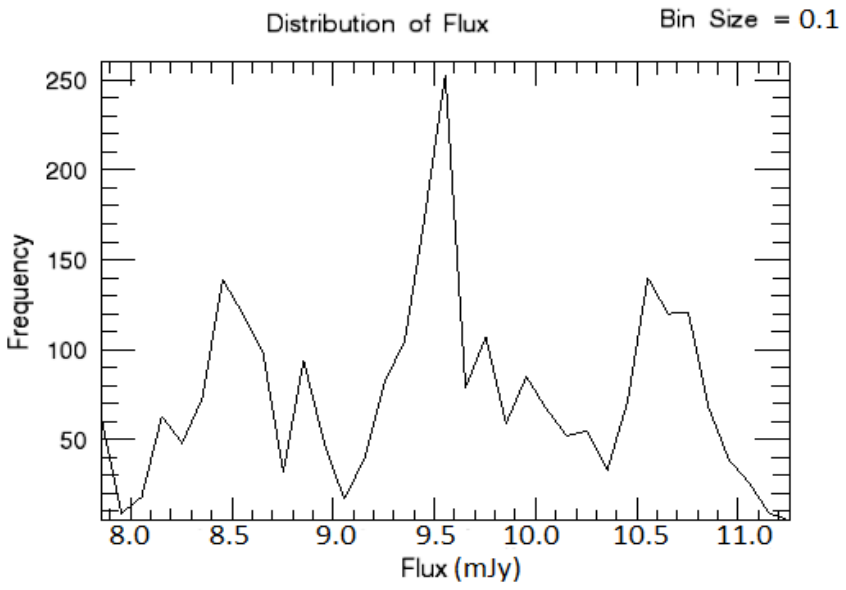

Figure 3.6: The flux distribution of the light curve.

microvariability curves needed to be longer in order to get enough data to determine whether the variations are the result of a deterministic stochastic process.

We repeated the same noise analysis reported by Dhalla et al. (2010) with the WEBT 72-hour light curve presented here. The data were binned into 45 minute bins and only bins with a minimum of 20 data points were used. Figure 3.6 shows the flux distribution for the 72-hour light curve. The horizontal axis represents the flux in millijansky (mJy) and the vertical axis the number of times a flux magnitude falls within the given bin of given magnitude. The lack of Gaussian form indicates we are not dealing with a simple Gaussian noise process. Figure 3.4 shows the RMS vs flux plotted for the bins, and it shows no significant linear relationship between RMS and flux (with a correlation coefficient of 0.0003). We then re-plotted the FT power spectrum in log-log space as shown in Figure 3.8, the DFT resembled $1/f^2$ noise. Prominent features remained in the data that were large deviations from a simple noise distribution.

3.4 Summary

As seen in section 3.2, the DFT results in various time scales, which, when compared with the results of other observers (Gupta, Srivastava, & Witta, 2009), do not lead to a

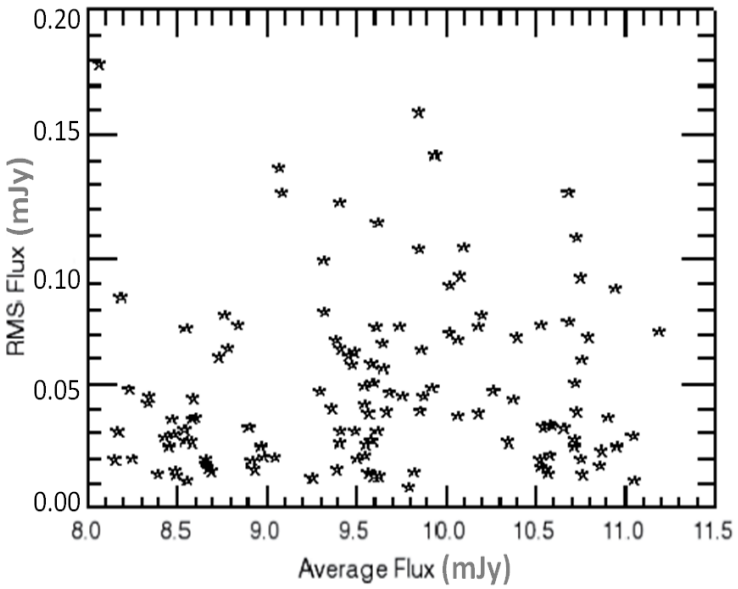

Figure 3.7: The RMS variations versus time for the entire 3-day observation.

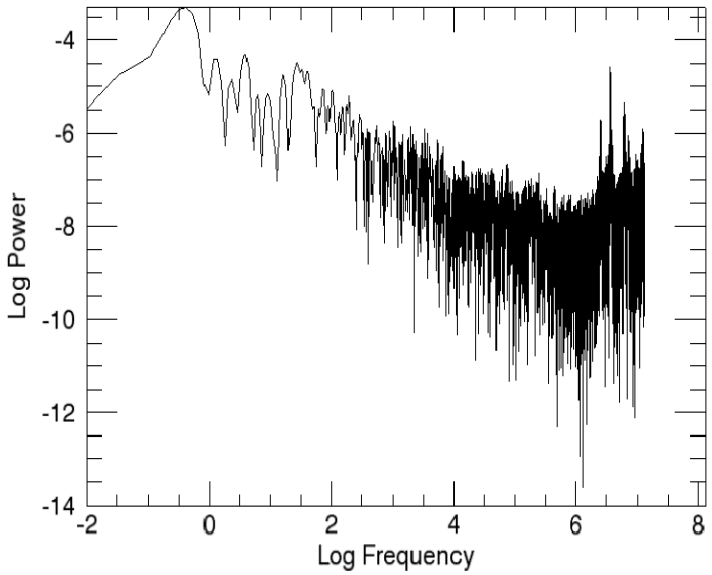

Figure 3.8: The log-log plot of the power spectrum of 0716.

consistent period. Simiarly, the period reported by the wavelet analysis is not supported by any similar other work. There seems to be some kind of structure in log-log space, but the analysis is inconlusive as to whether it arises from red noise like the realization of a stochastic processe, or an actual period. This leads us to the conclusion that time series analysis may not be the best approach to study in microvariabiliy. On the other hand, it can be seen from Table 3.1 that the maximum rise and decline in slope of the different sections in the light curve are similar to one another. This suggests a new approach for studying microvariability of blazars. We propose to interpret these as pulse emissions coming from an isolated or convolved turbulent regions in the blazar jet.

CHAPTER 4

The Pulse Model

4.1 Chapter Overview

This chapter outlines the modeling of the light curve in terms of a new model consisting of convolved shot pulses. Section 4.4 describes the theoretical model for the pulses generated when a plane shock encounters turbulent cells as it passes down the blazar jet. Starting with diffusion equations, we find an expression for the intensity emitted by cylindrical plane cells in the jet during and after the particles are accelerated to Lorentz factors of a few thousand. Section 4.5 presents the fitting of the light curve with the model pulses which then are converted into physical parameters guided by the theoretical model. The evaluation of these parameters is described in section 4.5.

4.2 Introduction

Because the jet of a blazar is oriented close to the line of sight, the non-thermal radiation from the jet dominates the thermal radiation from the accretion disk. Therefore it is believed that all of the variability properties we observe are associated with physical processes in the jet. Figure 4.1 shows a current model of a blazar jet by (Marscher, 2002). The model involves a shock wave passing through the jet flow and accelerating electrons to high energies. These shock waves accelerate the electrons, and compress, and therefore enhance the magnetic field to very high intensities. The particles then cool by emitting synchrotron radiation. The fiigure also shows various emitting regions including optical, IR, UV and X-rays in different colors.

Marscher & Gear (1985) explained outbursts as coming from shock waves passing through an adiabatic, conical, relativistic jet (Marscher & Gear, 1985). They also used this model to explain the production and evolution of superluminal knots seen in VLBI maps and the X-ray variability observed in 3C 273 and similar sources (Marscher & Gear, 1985). Kirk, Melrose, &Priest (1994) used plane shock waves passing through

a cylindrical jet to expain the spectral behaviour observed in Mkn 521. Sikora et al. (2001) assumed the individual shock events in the plasma material arise due to the velocity irregularities in the beam of the conical jet to explain the spectral behavior of X-ray and γ-ray flares (Sikora et al., 2001). Sokolov et al. tried to simulate the multi-frequency variability seen in 3C 273 by assuming that the observed flares are caused by the collision of the relativistic shocks with some stationary structures such as a Mach disk (Sokolov, Marscher, & McHardy, 2004).

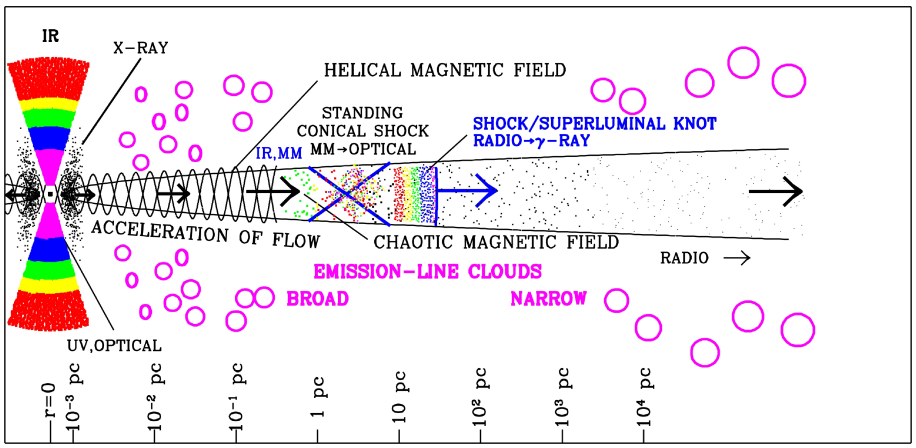

Figure 4.1: A current model of a blazar jet by Alan Marscher (Marscher, 2002). It shows the various emission regions at various distances from the central engine

As discussed in the previous sections, the passage of a shock wave through the blazar jet may result in a short term flare. Here we propose that when the flow in the jet is laminar we can see a flare but we do not see microvariability. When the flow of plasma material is turbulent, the shock wave excites individual cells in the jet and the synchrotron emission from each cell is a pulse of emission whose shape and size depends on the cell size, the local density enhancement, and the frequency of the emission. Figure 4.2 shows a graphic reprenstation of a turbulent relativistic jet. Each yellow circle represents a turbulent cell in the jet and the red line represents a strong shock which propagates down the jet and energizes the cells. The emission from these cells results in a synchrotron pulse.

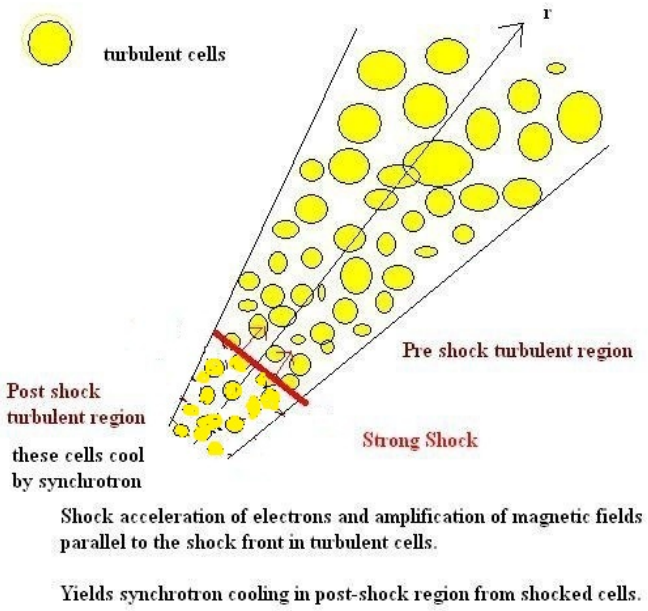

Figure 4.2: Synchrotron radiation from the shocked region of a Blazar jet.

4.3 Blazar Jets

Relativistic jets are common in extragalactic astrophysics. Most of the radio-loud AGN possess jets in the form of narrow streams of plasma. These jets are created and lauched near the black hole, and they extend to several parsecs where they deposit the power into double radio structures (Begelman, Blandford, & Rees, 1984). Jets can be seen in VLBI images resolved down to parsec scales. Jets can appear long or short, nearly straight or sharply curved, relatively smooth or knotty. In blazars, the jets are within several degrees of the line of sight so the beaming effects are strongly pronounced. As a result, they display superluminal apparent speeds, and projection effects can distort the apparent geometry in such a way that they appear fatter, shorter, and more sharply bent than they would if observed side-on.

According to the current picture, the jets are launched with differential rotation of the poloidal component of the magnetic field either in the inner disk or, for a rotating BH, in the ergosphere. The magnetic field then can accelerate the jet to high Lorentz factors

(Meier, Koide, & Uchida, 2000). The blazar jets tend to dominate the emission across essentially the entire electromagnetic spectrum. The emission is affected by relativistic beaming. The magnetic field and the electron injection rate are usually modeled as power laws and given by $K = K_1 r^{-n}$ and $B = B_1 r^{-m}$, where K_1 and B_1 are the electron injection rate and magnetic field at the apex of the jet (Konigl, 1981). The intrinsic opening angle of the jets are found to be inversely proportional to the Lorentz factor of the flow (Jorstad, 2005). The fastest AGN jets are found in γ-ray bright blazars (Kellermann et al., 2004; Piner, 2006). In a VLBA survey of about 60% of Energetic Gamma Ray Experiment Telescope (EGRET) sources identified as blazars, the highest reported apparent velocity is as high as 45c (Jorstad, 2001). Although most of knots in the jet move at apparent superluminal velocities, some are stationary or move at subluminal speeds (Jorstad, 2005).

Changes of the order of 10^o in direction of the blazar jets over time have been detected. When the effect of relativistic beaming is removed, this translates to less than $\sim 1^o$ which is still a large value for the momentum transfer. One possible explanation is that the swings in the jet direction could be caused by the precession of the jet due to two black holes orbiting each other at the center of the system. This configuration requires that the jet direction oscillates smoothly. However, evidences has been found that the jets of several blazars change direction more erratically than would be consistent with precession (Jorstad, 2005).

The estimation of energy contained in relativistic particles in the blazar jets requires various assumptions involving the intensity of the magnetic field present in the jet. There are mainly two methods of estimation. The first is to assume equipartition between the magnetic and particle energy densities. This case is similar to calculating the minimum energy required to produce synchrotron emission (Burbidge, 1959). The second method is to analyze compact knots that are synchrotron self-absorbed, in which case the energy density in radiating electrons and magnetic field can be determined separately (Marscher, 1983).

The jets are collimated by the differentially twisting magnetic fields emanating from

the ergosphere of the central black hole. Pair creation might be the dominant process that injects particles into the base of the jet (Meier, Koide, & Uchida, 2000). The photons from the accretion disk and corona can enter the jet and pair-produce off the strong magnetic field. Whether the jet is accelerated to a high bulk Lorentz factor close to the central engine or over a distance of hundreds or thousands of gravitational radii is still debatable. In gas dynamical models the acceleration and focusing of the jet occur over an extended distance (Marscher, 1980; Vlahakis, & Knigl, 2004). It is also unclear whether the particles in the jet consist of electrons and protons, pair plasmas, or a combination of the two. This becomes a crucial issue, as the composition of a jet is intimately linked to the physical processes that create and energize it (Blandford & Levinson, 1995; Sikora, & Madejski, 2000).

4.4 A New Model

Kirk, Reiger, & Mastichiadis (1998) tried to explain a short term flare in Mkn 521 by assuming a shock wave moving along a cylindrical jet interacts with a density-enhanced regions of a uniform magnetic field. The shock accelerates the electrons which then cool by emitting synchrotron radiation. We adopt this model to explain microvariability seen in the WEBT microvariability curve of 0716+714. Our model interprets the microvariability as emission from turbulent cells in the jet by using the same basic mathematical structure. We adapted the model to account for the change in optical flux in very short time scales. Since the new model is based on the model by Kirk, Reiger, & Mastichiadis (1998), a detailed mathematical discussion of this model, altered for our purposes, is presented below.

The model considers a cylindrical jet consisting of basically two regions: the acceleration zone and the emission zone. The plane perpendicular shock waves interact with the electrons in the acceleration zone at a particular energy γ_0, accelerating the electrons to maximum energy γ_{max}, and creating a distribution of particle energies governed by

the diffusion equation

$$\frac{\partial N}{\partial t} + \frac{\partial}{\partial \gamma}\left[\left(\frac{\gamma}{t_{acc}} - \beta_s \gamma^2\right)\right] N + \frac{N}{t_{acc}} = Q\delta(\gamma - \gamma_0). \tag{4.1}$$

The first term in square brackets gives the acceleration of the particles and the second term represents the loss of the energy by the synchrotron radiation (Rybicki & Lightman, 1979) ,

$$\beta_s = \frac{4}{3}\frac{\sigma_T}{m_e c^2}\left(\frac{B^2}{2\mu_0}\right), \tag{4.2}$$

with σ_T, B and μ_0 the Thompson's scattering cross section, the magnetic field, and the permeability of free space, respectively. The differential equation 4.1 can be solved using the Laplace transform method. We get

$$N(\gamma, t) = a\frac{1}{\gamma^2}\left(\frac{1}{\gamma} - \frac{1}{\gamma_{max}}\right)^{(t_{acc}-t_{esc})/t_{esc}} \times \Theta\left(\gamma - \gamma_0\right)\Theta\left(\gamma 1\left(t\right) - \gamma\right), \tag{4.3}$$

with $\gamma_0 < \gamma < \gamma 1\left(t\right)$ and $N(\gamma, t) = 0$, otherwise. In equation 4.3, $\Theta\left(\gamma - \gamma_0\right)$ and $\Theta\left(\gamma 1\left(t\right) - \gamma\right)$ are the Heaviside step functions, and a is given as,

$$a = Q_0 t_{acc} \gamma_0^{t_{acc}/t_{esc}} \left(1 - \frac{\gamma_0}{\gamma_{max}}\right)^{-t_{acc}/t_{esc}}. \tag{4.4}$$

The upper bound for the energy of the particles is governed by the equation,

$$\gamma 1\left(t\right) = \left(\frac{1}{\gamma_{max}} + \left[\frac{1}{\gamma_0} - \frac{1}{\gamma_{max}}\right] e^{-t/t_{acc}}\right)^{-1}, \tag{4.5}$$

with $\gamma_{max} = \left(\beta_s t_{acc}\right)^{-1}$. The quantities t_{acc} and t_{esc} are assumed to be fixed and independent of the energy. Once the particles are accelerated in the acceleration zone, they escape to the downstream plasma where they lose most of their energy by emitting synchrotron radiation. This region of the jet, therefore, forms the emission zone as discussed earlier. The moving shock wave injects the accelerated electron into the

emission zone and the evolution of particle density in this zone is given by the following partial differential equation:

$$\frac{\partial n}{\partial t} - \frac{\partial}{\partial \gamma}\left(\beta_s \gamma^2 n\right) = \frac{N(\gamma, t)}{t_{esc}} \delta\left(x - x_s(t)\right), \tag{4.6}$$

where $x_s(t)$ is the position of the shock front at time t. The shock accelerates the particles at time $x = 0$ and $t = 0$ and moves with a constant speed u_s. According to the solution of Equation 4.6,

$$\begin{aligned} n\left(x, \gamma, t\right) = \quad & \frac{a}{u_s t_{esc} \gamma^2}\left[\frac{1}{\gamma} - \beta_s\left(t - \frac{x}{u_s}\right) - \frac{1}{\gamma_{max}}\right]^{(t_{acc} - t_{esc})/t_{esc}} \\ & \times \Theta\left[\gamma 1\left(x/u_s\right) - \left(1/\gamma - \beta_s t + \beta_s x/u_s\right)^{-1}\right] \end{aligned} \tag{4.7}$$

when the density function is convolved with Green's synchrotron function integrated with the γ for a particular frequency, we get the synchrotron emission from the region. Green's synchrotron function is given by

$$P(\nu, \gamma) = a_s z^{0.3} exp(-z), \tag{4.8}$$

where $a_s = \frac{\sqrt{3} e^2 \Omega sin\theta}{2\pi c}$ is a constant, and $z \equiv 4\pi\nu / \left(3\Omega sin\theta \gamma^2\right)$, with $\Omega = \frac{eB}{m}$ the electron gyro frequency, and θ the angle between the magnetic field direction and the line of sight. The intensity of the synchrotron emission is given by

$$I_0\left(\nu, t\right) = \int\int P\left(\nu, \gamma\right) n\left(x, \gamma, \bar{t} + x/c\right) dx d\gamma. \tag{4.9}$$

The integrated particle density is given by

$$\int n(x,\gamma,t)dx = \frac{a}{(1-\frac{u_s}{c})\gamma_{(max)}^{(t_{acc}+t_{esc})/t_{esc}}}(\frac{\gamma_{max}}{\gamma})^2 \times \left\{[\frac{\gamma_{max}}{\gamma} - \frac{t}{t_{acc}} + \frac{x(1-u_s/c)}{u_s t_{acc}}]^{t_{acc}/t_{esc}}\right\}_{x_0(\gamma,t)}^{x_1(t)} \tag{4.10}$$

The upper limit of the spatial integration is given by the position of the shock wavefront given by

$$x_1(t) = \frac{u_s}{1-u_s/c}, \tag{4.11}$$

whereas the lower limit is given by the cooling length

$$x_0(\gamma,t) = Max\left[x_{cool}\left(\gamma,t\right), x_1(t) - L\right], \tag{4.12}$$

where x_{cool} is obtained by solving the transcendental equation

$$\left[\frac{\gamma_{max}}{\gamma} - \frac{t + x_{cool}/c}{t_{acc}} + \frac{x_{cool}}{u_s t_{acc}}\right] = 1 + \left(\frac{\gamma_{max}}{\gamma} - 1\right) exp\left[-x_{cool}/\left(u_s t_{acc}\right)\right]. \tag{4.13}$$

In this equation $x_1(t) - L$ represents the maximum spatial extent of the emission region, with

$$L = \frac{t_b u_s}{1-u_s/c}. \tag{4.14}$$

The particle enhancement in the regions is described by the equations

$Q\left(t\right) = Q_0$ for t<0 and t>t_f and $Q\left(t\right) = \left(1+\eta_f\right)Q_0$ for 0<t< t_f,

which then leads to

$$I\left(\nu,t\right) = I_1\left(\nu,t\right) + \eta_f\left[I_1\left(\nu,t\right) - I_1\left(\nu,\left(1-u_s/c\right)t_f\right)\right]. \tag{4.15}$$

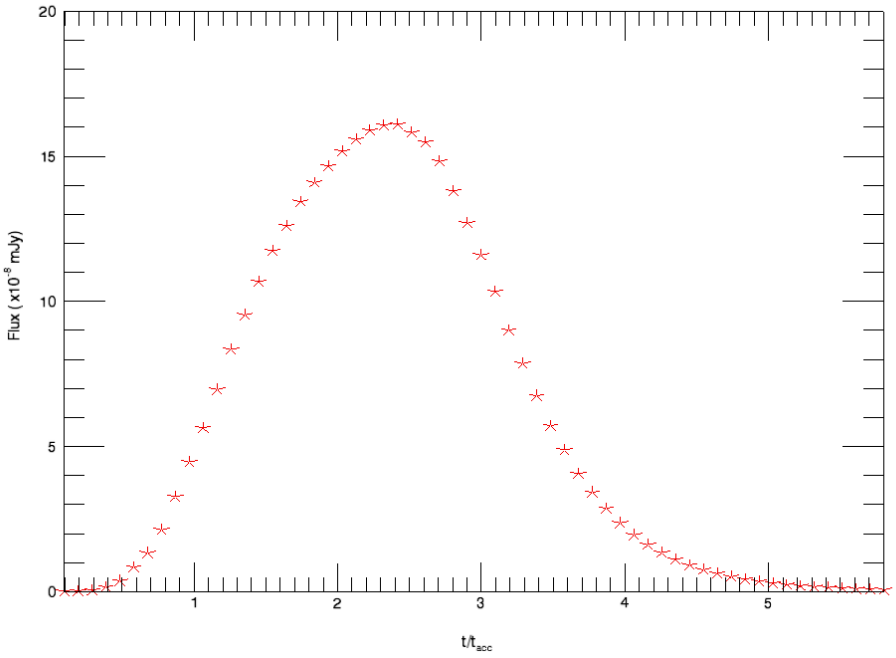

Figure 4.3: Pulse resulting from Eq. 4.15 with B=2 Gauss, Q = 609.3 m^{-3} s^{-1}, optical frequency $\nu = 4.3 \times 10^{14}$ Hz and $t_f = 2.5/t_{acc}$.

The variation of flux with time in the optical frequencies as given by Equation 4.15 is shown in Figure 4.3. This represents the pulse that we used to fit the light curve. Based on the frequency and the duration of the flare different pulse shapes can be obtained from the model. Two such pulses are shown in Figure 4.4.

As we are dealing with the blazar jet, which is very far away (high redshift) and hence is early in time, and which is moving relativistically toward us with tremendous speeds, relativistic corrections and the cosmological correction have to be made the quantities in the rest blazar frame. The relativistic correction in this case is in the form of the Doppler factor which is given by (Khembhavi & Narlikar, 1999),

$$Doppler\ Factor = \frac{1}{\Gamma\left(1 - \beta cos\varphi\right)} \tag{4.16}$$

where Γ, βc and φ are bulk Lorentz factor, velocity and angle with the line of sight of the jet respectively. If we combine the relativistic correction with the cosmological

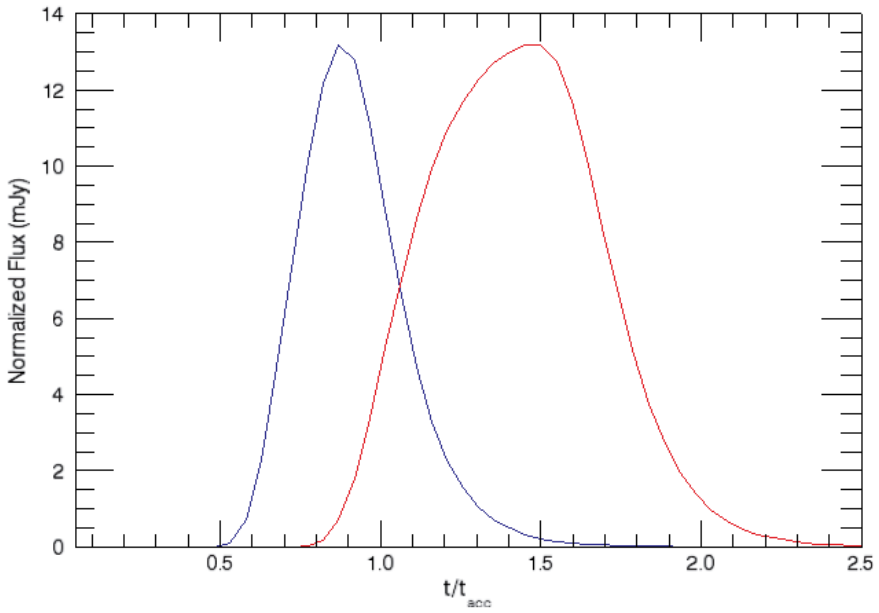

Figure 4.4: Pulse shapes for frequencies $\nu = 4.3 \times 10^{16}$ Hz (blue) and $\nu = 4.3 \times 10^{17}$ Hz (red) from Eq. 4.15 with B=2 Gauss, Q = 609.3 m^{-3} s^{-1} and time of flare $t_f = 1.25/t_{acc}$.

correction, the total correction factor is given as

$$Correction\ Factor = \frac{z}{\Gamma\left(1 - \beta cos\varphi\right)}. \tag{4.17}$$

where z is the redshift of the blazar. Therefore the transformation equations for frequency, time and light flux from the source frame of reference to the observer's frame of referenc are given by

$$t_s = \frac{z+1}{\Gamma\left(1 - \beta cos\varphi\right)} t_o, \tag{4.18a}$$

$$\nu_o = \frac{z+1}{\Gamma\left(1 - \beta cos\varphi\right)} \nu_s, \tag{4.18b}$$

$$I_o = \left(\frac{z+1}{\Gamma\left(1 - \beta cos\varphi\right)}\right)^3 I_s, \tag{4.18c}$$

where subscript o and s denote observed and source quantities, respectively.

4.5 Fitting Pulses

According to our model, each of the structures in the light curve corresponds to the interaction of a relativistic shock wave with the density- enhanced region of the jet. This causes the observed microvariability, representing the turbulent nature of the emission regions in the jet. It is assumed that the laminar flow in the jet is not the cause of these very short fluctuations. Therefore, for a true microvariation, the short term and long term variability have to be subtracted. Hence, the minimum flux was taken as the baseline above which the microvariation stuctures were considered to be superimposed. The resulting light curve then was treated as convolutions of the pulse emissions from inhomogenous cells of various size and density enhancements. For every local peak in the light curve, its location was taken as the center position of the cell, its amplitude as the degree of the density enhancement, and its width as its spatial extension.

Calculations

The following parameters were used for the calculation of the pulse shape. Input Parameters:

Minimum electron energy(γ_0)=10

Maximum electron energy (γ_{max}) = 1000

Magnetic field (B)= 2 Gauss

Direction of Magnetic Field (θ) = $\frac{\pi}{2}^o$

Shock speed (β_s) = 0.1 (from Kirk, Reiger, & Mastichiadis (1998))

Bulk Lorentz Factor of the jet (Γ)=17 (from Celotti & Ghisellini Celotti, & Ghisellini (2008))

Calculated Parameters

$\Omega = \frac{eB}{m} = 3.51 \times 10^7$ Hz

$\beta_s = \frac{4}{3}\frac{\sigma_T}{m_e c}\left(\frac{B^2}{2\mu_0}\right) = 5.16 \times 10^{-9}$ s

$t_{acc} = \frac{1}{\beta_s \gamma_{max}} = 1.9 \times 10^5$ s

$a_s = \frac{\sqrt{3} e^2 \Omega sin\theta}{2\pi c} = 2.26 \times 10^{-41}$

$z = \frac{4\pi}{3\Omega sin\theta} \frac{\nu}{\gamma^2} = 4.34 \times 10^{-6} \frac{\nu}{\gamma^2}$ Hz^{-1}

Baseline in the curve that represent the back-ground flux (I_0) =7.85 mJy (from the light curve)

Orientation of the jet axis (φ)= 2.6^o (from Celotti, & Ghisellini (2008))

Calculation of the back-ground intensity

The baseline in the curve that represents the minimum flux determined from the light curve was I_0=7.85 mJy. This observed back-ground flux was then converted to the flux in the rest frame of the blazar by the transformation

$$I_s = \left(\frac{z}{\Gamma \left(1 - \beta cos\varphi\right)} \right)^{-3} I_o.$$

With the parameters listed above, the factor of transformation was calculated to be $\left(\frac{z}{\Gamma(1-\beta cos\varphi)} \right)^3 = 4409.98$. Using Equation 4.15 for $t = 500 t_{acc}$ (a large value) for the constant laminar flow the density for the minimum flux was estimated to be Q_0= 609.3 s^{-1} m^{-3}.

Calculation of the particle injection number for various cells

Once the back-ground density was estimated, any peak in the light curve was interpreted as a density enhancement above the back-ground level. This can be calculated using the relation

$$Q_{enhanced} = \frac{I_{amplitude}}{I_0} \times Q_0,$$

where $I_{amplitude} = I - I_0$, the intensity of the local peaks above the back-ground intensity.

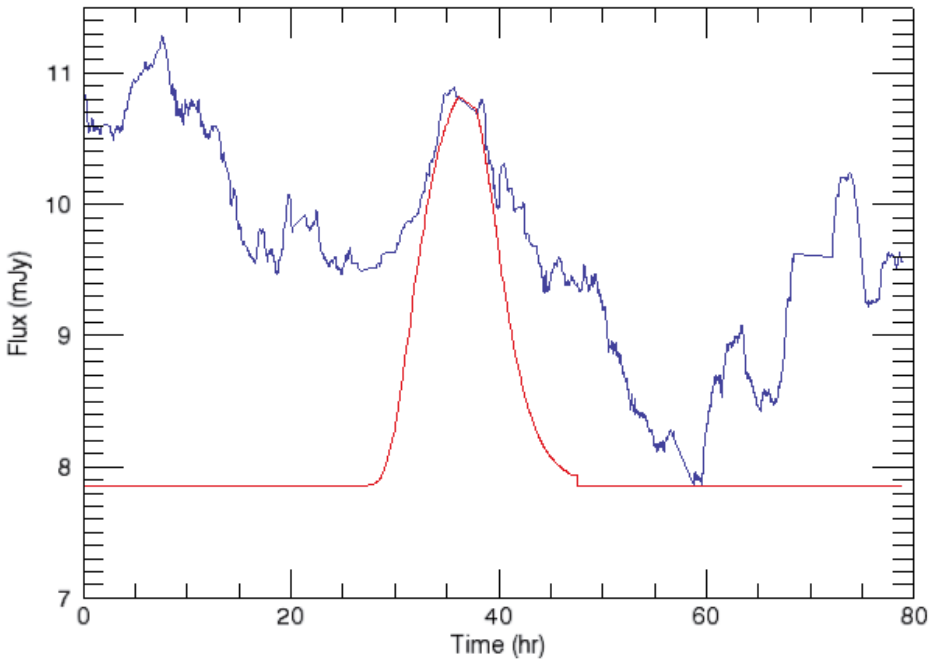

Figure 4.5: An example of fitting a peak at 36.5 hours with amplitude of 2.99, and width of 3.71 hours width using a pulse obtained from the model.

Calculation of the cell sizes

The width of the pulse of emission correspond to the size of the particular cell by the relation

$$cellsize = t_{flare} \times \beta c.$$

The velocity of the shock wave was chosen to be $\beta = 0.1c = 3 \times 10^7$ m s^{-1}. Multiplying the velocity with the time during which the density enhancement occurs, estimated to be $t_{flare} = \frac{1}{2}\times$ pulse width, gives the size of the cell.

An example of fitting a single peak at the center 36.5 hours with an amplitude of 2.99 mJy and 3.7 hours width in the light curve is shown in Figure 4.5. The minimum flux of 7.85 mJy was taken as the back-ground flux representing longer timescale variability. Thirty-five pulses of various amplitude and width at different times of the light curve were convolved to fit the data with high precision. All the fitting parameters including the number of pulses, amplitude, width and location were selected so as to achieve a

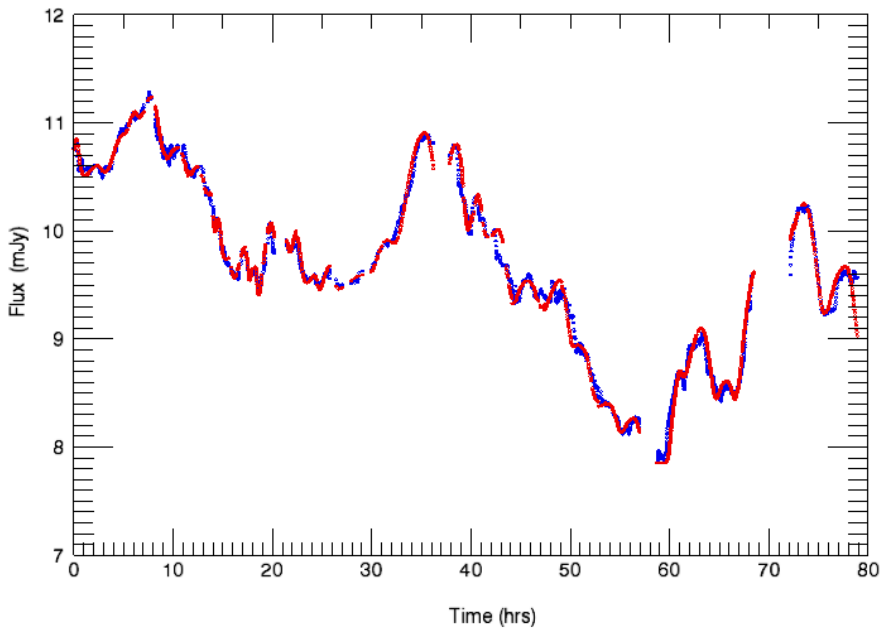

Figure 4.6: The light curve fitted with the pulses of amplitudes and widths listed in the table. The blue symbols are the data, and the red symbols represent the model.

high correlation coefficient, and a maximum number of degrees of freedom (the number of independent variables) given tby $(n_{pts} - (35 \times 3) - 1)$. The injection rate and the flare time were varied to change the amplitude and width of the pulses at different locations of the curve. A fitting of the entire light curve with 2,507 of degrees of freedom and a correlation coefficient of 0.98 is shown in Figure 4.6. The injection rates, flare times and locations of the flares which were used to model the data are listed in Table 4.1. The first column of the table lists the index number of the pulse, column 2 and 3 present the center and the amplitude of the pulses. Column 4 gives the half width of the pulse, which translates to the time of enhanced injection (flare). Error in the amplitudes and pulse widths are listed in column 5 and 6 respectively. The errors were estimated by changing the variables so that the correlation coefficient would become less than 95%. The amplitude of the pulse is then converted to the enhanced injection rate of electrons in the cell as listed in the column 7. Cell sizes are computed by multiplying the time of the flare by shock velocity, and are presented in column 8.

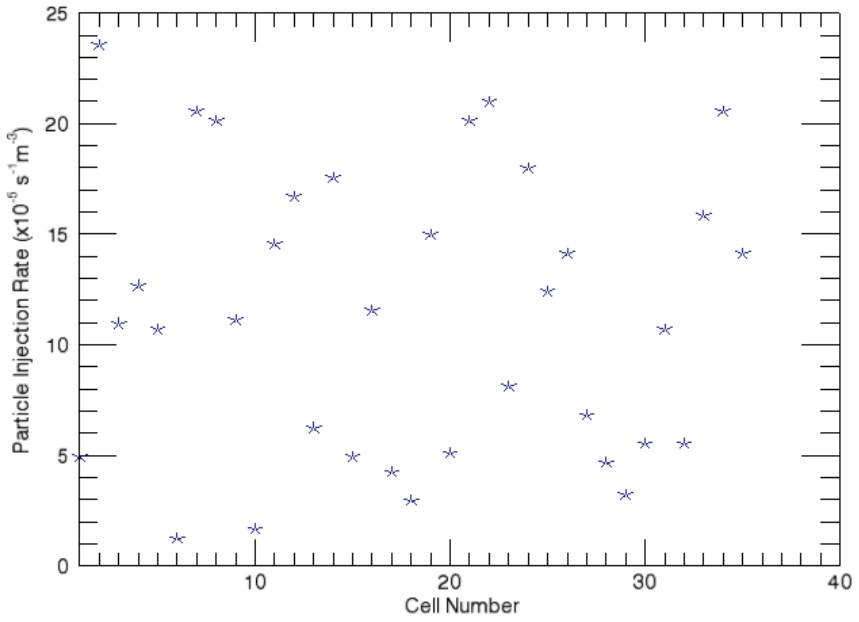

Figure 4.7: The distribution of particle injection rates in the cells of turbulent regions as the shock moves down the blazar jet.

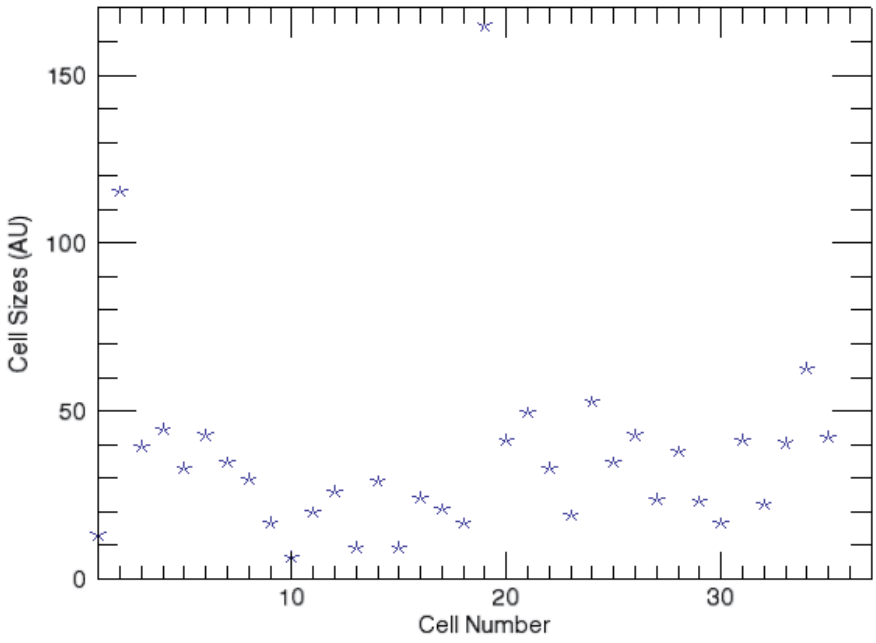

Figure 4.8: The distribution of the cell sizes of the turbulent regions as the shock moves down the blazar jet.

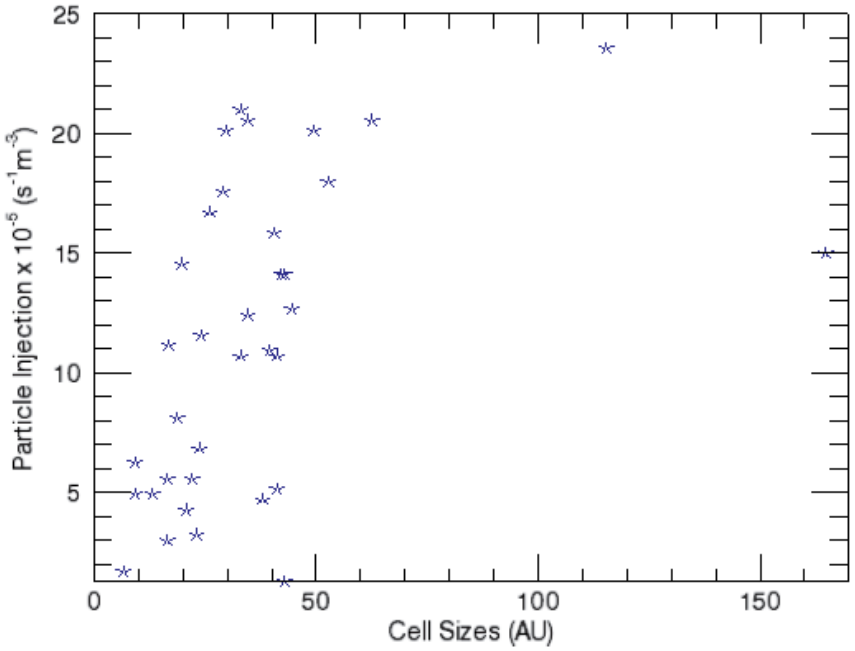

Figure 4.9: The distribution of particle injection rates in the cells versus turbulent region cell sizes.

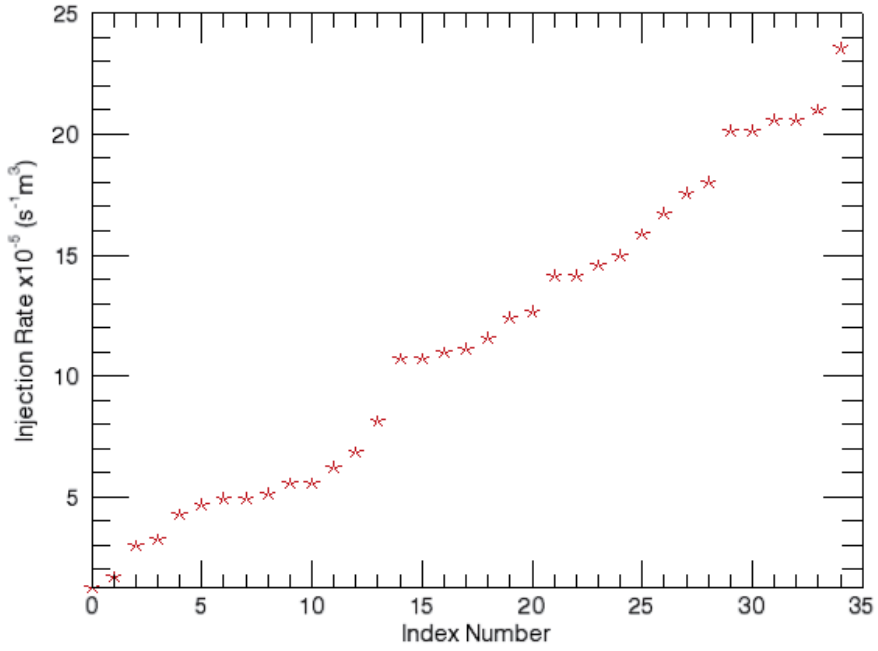

Figure 4.10: The distribution of cells over particle injection rates.

Pulse	Center (hr)	Amp (mJy)	τ_{flare} (hr)	Amp. Err. $\times 10^{-3}$ (mJy)	$\tau_{flare}Err.$ $\times 10^{-3}$(hr)	N$\times 10^{-5}$ (s^{-1} m^{-3})	S_{cell} (AU)
1	0.15	0.57	1.11	1.4	4.2	4.94	13.18
2	2.10	2.74	9.74	9.2	7.9	23.56	115.35
3	5.70	1.27	3.34	9.6	6.6	10.94	39.54
4	7.80	1.47	3.75	0.4	8.5	12.66	44.49
5	8.45	1.24	2.78	9.3	6.8	10.69	32.95
6	10.80	0.14	3.61	7.6	7.4	1.25	42.84
7	10.90	2.39	2.92	3.9	6.6	20.56	34.60
8	13.00	2.34	2.50	1.9	7.1	20.13	29.66
9	14.30	1.29	1.41	0.3	2.8	11.12	16.80
10	14.60	0.19	0.55	0.5	1.0	1.68	6.59
11	15.50	1.69	1.67	8.2	6.9	14.55	19.77
12	17.20	1.94	2.19	3.2	9.5	16.69	26.03
13	18.20	0.72	0.78	0.3	4.4	6.22	9.22
14	19.75	2.04	2.45	3.8	7.7	17.55	29.00
15	21.30	0.57	0.78	8.0	1.9	4.94	9.22
16	22.30	1.34	2.03	4.9	4.5	11.55	24.05
17	24.10	0.49	1.75	6.5	7.1	4.25	20.76
18	25.65	0.34	1.39	7.5	2.8	2.96	16.47
19	29.10	1.74	13.91	6.8	6.6	14.98	164.79
20	32.40	0.59	3.47	1.6	1.2	5.11	41.19
21	35.55	2.34	4.17	5.0	9.6	20.13	49.43
22	38.69	2.44	2.78	3.4	5.9	20.99	32.95
23	40.55	0.94	1.58	2.2	7.5	8.11	18.78
24	42.60	2.09	4.45	2.6	5.1	17.98	52.73
25	45.95	1.44	2.92	7.0	8.9	12.40	34.60
26	48.90	1.64	3.61	9.6	5.5	14.12	42.84
27	51.40	0.79	2.00	1.4	1.5	6.83	23.73
28	53.75	0.54	3.20	2.6	8.4	4.68	37.90
29	56.40	0.37	1.94	2.5	8.1	3.22	23.07
30	60.80	0.64	1.39	2.4	9.3	5.54	16.47
31	63.10	1.24	3.48	3.5	2.0	10.69	41.19
32	65.85	0.64	1.86	2.5	6.2	5.54	22.08
33	68.80	1.84	3.42	4.7	3.5	15.84	40.53
34	73.40	2.39	5.28	8.3	5.9	20.56	62.62
35	77.80	1.64	3.56	5.5	9.2	14.12	42.18

Table 4.1: Pulse parameters used to fit the data

The resulting injection rates and cell sizes for each of the peaks in the light curve, as listed in the 5th and 6th column of Table 4.1 are plotted in Figures 4.7 and 4.8, respectively. The fiigures show that they do not follow any preferred spatial or temporal distribution. However, when the distribution of cells over sizes was plotted in Figure 4.11, it could be seen that most of the cell sizes are limited to within 5 to 60 AU. This indicates that the jet environment does not favor the formation of larger turbulent regions. A turbulence analysis of the result is discussed in the following section.

4.6 Turbulent Analysis

Turbulent regions in relativistic jets have natural length scales known as integral length scale which is about the size of the largest turbulent regions formed in the jets. These largest region are unstable and break into smaller regions until the energy contained in them is dissipated away by the viscous forces (Pope, 2000). The size ranges of the turbulent regions are crudely divided into three classes. The largest regions are the energy containing size ranges and they are characterized by integral length scale. The middle-size ranges are inertial subranges which transport energy from largest regions to the smallest ones known as dissipative size ranges. The smallest regions are characterized by Kolmogorov length scale which contain information about viscous forces present in the plasma material of the jets (Falkovich & Sreenivasan, 2006). The smallest resolved turbulent cell size obtained by our modeling is ~ 6 AU. We interpret the smallest size as the Kolmogorov length scale which appears on the Reynolds number expression

$$Re_\eta = \frac{\eta u_\eta}{\nu} \tag{4.19}$$

where Re_η, η, u_η, and ν are Reynolds number, Kolmogorov length scale, Kolmogorov velocity scale and kinetic viscosity of the plasma material. Using the various estimates for the Reynolds number and the velocity for turbulence in relativistic jets, we can estimate the viscosity of the plasma material in the jet (Smith, 2012). In this case, the study can provide important informations about conditions in the relativisic jets. Similarly, as

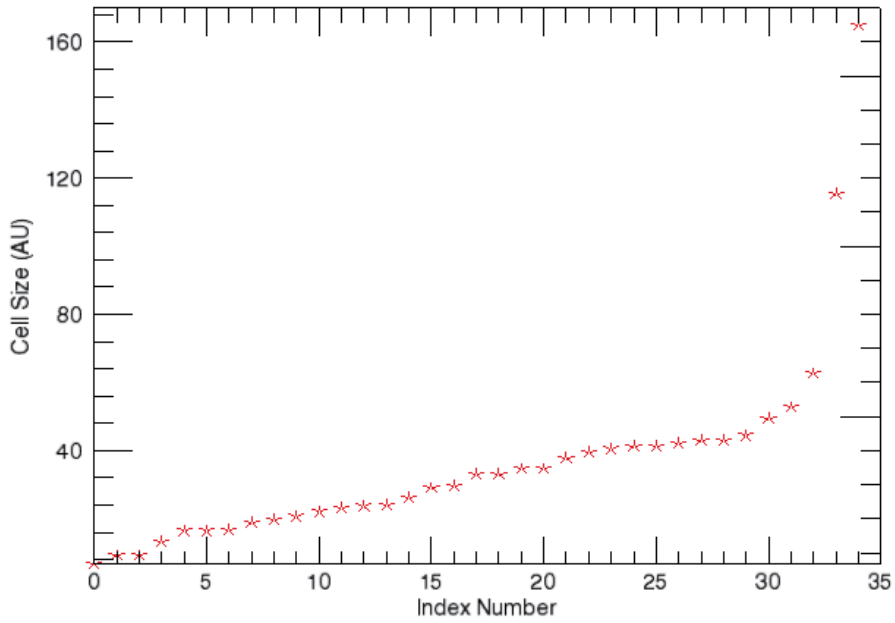

Figure 4.11: Distribution of cells over cell sizes as listed in Table 4.1.

we can see from Figure 4.11 that most of the cell sizes are limited within 60 AU, this distribution of the cell sizes can be interpreted as a range of stable turbulent regions. This provides an estimation of the demarcation line between the energy containing range and internal subrange. This has important implication in the understanding of the energy contained in the turbulent cells and the possible energy transportation mechanisms. This also provides an explanation to the fact that there few cell sizes above 60 AU, as they become unstable. The injection rate for cells versus corresponding cell sizes are plotted in Figure 4.9. However, no correlation between them was observed.

4.7 Summary

A new model based on mathematical formulation of Kirk, Reiger, & Mastichiadis (1998) was developed. The model described thesymmetrical structures in the light curve as resulted by the pulse emission in the relativistic jet of the blazar. The model fitted the data very well, with a Pearson's correlation coefficient of 0.98 and yielded some of the physical parameters and the sizes of the cells of the turbulent regions in the jet. Some

of the important implications and conclusions of these results are discussed in the next chapter.

CHAPTER 5

Summary and Conclusions

5.1 Chapter Overview

This chapter presents a summary of the works, and discusses the results obtained from the modeling of the light curve obtained by the WEBT campaign. We also indicate some of the directions the model might take in future works.

5.2 The WEBT Campaign and the Light Curve

The main objective was to model the light curve of 0716+714 from the WEBT campaign of 2009, and to shed light on the nature of microvaribility in blazars. Overlap in the data contributed by observers from various sites bolster the idea that the phenomenon of microvariability is intrinsic to a source, as opposed to being an instrumental or environmental effects. As the non-thermal emission from the source and short time-scale variations in the flux are believed to come from the jets, the study of microvariability leads to the investigation on the turbulent nature of blazar jets. The idea was to reproduce the observed patterns in the lightcurves which include milli-magnitude flux changes within time-scales of few minutes to hours. Higher order fluctuations were considered to be related the Possion noise associated with the instruments, the camera and the atmospheric conditions.

Time series and noise analyses of the data did not reveal any true periodicity within the given timescale. Previous lightcurves were limited by the length of the night time at the site. But the discrete Fourier transform and the wavelet analysis yielded periods consisting of only two cycles hence were unreliable. The DFT gave various periods of various time scales making the periodicity search unreproducible from one light curve to the next. Since the time series analysis did not yield a consistent period, the next obvious step was to see if the light curve reflected any kind of stochastic noise process, in particular red noise noise processes. The stuctures obtained from the DFT analysis

were far above the noise level. This indicated that the emission processes taking place in the blazar were not completely random. The similarity between the rate of rise and fall in individual structures in the light curve motivated us to analyze these stuctures in the light curve. That is how the idea of the modeling the entire light curve as the convolution of a series of the pulses was conceived. This method of analysis is original and new in the field.

5.3 The Modeling and Results

A model based on individual rapid synchrotron pulses caused by a shock wave encountering individual turbulent cells in the jet flow was developed. The mathematical description of the process was based on model due to the KRM for X-ray flares in AGN jets. The diffusion equations were solved describing enhanced particle acceleration at relativistic shock fronts in a cylindrical jet. This required the solution of the associated transcendental equation for the calcultion of cooling length of high energy particles using computer program Interactive Data Language (IDL). The resulting emission due to a cylindrical distribution of cells containing particles with Lorentz factors of thousands was calculated. A given value of electron enhancement that would last for a finite time results in a pulse of emission. Using thirty-five pulses of various sizes and intensities, I was able to fit the 72-hour nearly continuous flux curve in terms of this model, and obtain an estimate of the range of sizes of the turbulent cells and the density enhancements. It was found that the size of the vortex region and the magnetic field orientation of the turbulent cells were stochastic, and also the particle injection seemed to be sporadic. Similarly, no correlation was found between the cell sizes and the particle enhancement over the cells. But I found that we can decompose the microvariability curve into individual pulses and can get a picture of the underlying turbulent structure. The results also support our initial assumption that though a laminar flow of the plasma across the enhanced magnetic field may lead to a short term flare seen in the light curve, the turbulent flow results in very short-term microvariations.

The smallest resolved size of the turbulent regions found to be $\sim$ 6 AU and is as-

sumed to be the Kolmogorov length scale in the relativisic plasma. With the knowledge of Reynolds number and the velocity of the cells, we can estimate viscosity of the plasma material of the jet. Similarly, distribution of stable cell sizes found less than 60 AU, places an important contraint on the magnetohydrodynamic models. It provides an estimation for the demarcation line between the energy containing range and internal subrange. If an estimation for natural length scale and inertial subrange scale found from other works, this has important implication in the understanding of the energy contained in the turbulent cells and the possible energy transportation mechanisms between the interacting cells. In this case, the study can provide one of the most important informations about the plasma condition in relativisic jets

5.4 Future Work

The model explains the phenomenon of microvariability in blazar light curves as caused by particle accelerations due to a shock wave encountering turbulent jet flow. We have made various assumptions and kept various parameters fixed to keep the model simple. This leaves a lot of room for improvement to make the model more constraining and better fitting. Following the line of the models there are a couple of improvements to the theory and the following lists lists a few of them.

- The KRM model predicts change in the spectral shape as a function of time and flux during the flare. This feature of the model can serve as one of the tests against the model. To test the model we can conduct a simultaneous and multi-color campaign on a blazar to actually observe the behavior of the spectral index over the course of a single pulse.

- The magnetic field value for the cells is assumed fixed as suggested by the homogenous model. In the future, the magnetic field can be varied as a fuction of the radius of the jet. This would result in various pulse shapes corresponding to various values of the magnetic fields, and consequently to a better fit of the data with fewer degrees of freedom.

- Similarly, the ratio of the accelertion and the escape time, which has been kept fixed in this model, can be made a function of γ, making the model more realistic in spite of the mathematical complexity.

- The current model only takes into account the synchrotron emission due to high energy electrons in the jet. Other emission processes such as inverse Comption emission and pair production can be incorporated. The model also ignores the photon density, external and internal, in the source equation.These can be included in a more elaborate model.

APPENDICES

A IDL Program to Generate the Pulse

; This program creates a pulse corresponding to the particle enhancement equation 4.15
Pro Make_pulse, Flare,Tm

COMMON parameters,gama_max,gama_not,cs,us,tacc ; Common parameters shared by the program and the function below

;/ constants/

amp=5.0 ; A normalization number of the amplitude of the pulse
B=1.0e-3/amp ; Maganetic field
cs=3.0e+8 ; Speed of light
us=0.1*cs; Speed of shock
rho_T= 6.65e-29 ; Thompson scattering constant
m_e=9.1e-31 ; Mass of electron
mu_0=!pi*4.0e-7 ; Pearmeability for free space
gama_not = 10.0 ; Minimum Lorentz factorof the electrons
gama_max=1000.0 ; Maxmimum Lorentz factor of the electrons
beta_s = 4.0/3.0*rho_T(m_e*cs)*(B$\hat{2}$/(2*mu_0)) ; A constant in the KRM equations
tacc=1/(gama_max*beta_s) ; accelaration time
tesc=2.0*tacc ; escape time
Q=609.31; A normalise particle injection rate for the back ground intensity and divided by 2 for the fact that the injection is enhanced by a factor of 2

data_length=gama_max-gama_not ; the difference between the maximum and minimun Lorentz factors of the electrons
data_interval=0.5
data_nums=data_length/data_interval

```
power=(tacc-tesc)/tesc
pwr=(tacc+tesc)/tesc
a=Q*tacc*gama_not^(tacc/tesc)*(1-gama_not/gama_max) ; a constant is equation 4.5
factor = 1/gama_not -1/gama_max
as=4.1e-36*B
Nu=4.3e14; Optical frequency for the R filter

time=50 ; Time arrry
tm=fltarr(Time)
t_m=fltarr(Time)
Flux=fltarr(Time)
Flux2=fltarr(Time)
Intensity=fltarr(Time)

For k=0,Time-1 do begin tm(k)=(k+1.0)*tacc*0.1 ; Time loop
t=tm(k)
x1= t*us/(1-us/cs) ; Position of shock wave front
gama1=1/(1/gama_max+factor*exp(-t/tacc)) ; Instantaneous Larentz factor given by the
equation 4.5
;print,"gamma1 is",gama1

    ;/This part of the program ensure that incoming gamas are less than
; /gama1

r=gama_not+findgen(data_nums+1.0)*data_interval
;print,r y1=where(r lt gama1,count) ; Finds the total number of elements statisfying the
condition
gama=fltarr(count)
gama=r(0:count-1); Creating subarray from r
```

```
;print,gama

    ;/New variables declarations

N=fltarr(count); particle density
sync_func=fltlarr(count) ; Green's synchrotron function given by the equation 4.8
z=fltarr(count) ; A term is the equation 4.8
P=fltarr(count)
F=fltarr(count) ; Flux given by the equation 4.9

    ;/This part of the program calculates the flux

For i=0,count-1 do begin
;Length=(t-tb)/(1-us/cs)
x0=transcedental(gama(i),t)*us*tacc ; Cooling length calculate by the transecdental function
N1= a*gama_max^2/(0.9*gama_max^wr*gama(i) ^2)*(gama_max/gama(i)-t/tacc+x1*(1-us/cs)/(us*tacc)-1)^(tacc/tesc) ; Number density at the shock wave front
N0= a*gama_max^2/(0.9*gama_max^wr*gama(i)^2)
*((gama_max/gama_not-1)*exp(-x0))^(tacc/tesc)
;Number density at the end of the cooling length
N(i)=N1-N0
z(i)=23.8e-13*Nu/gama(i)^2
P(i)=as*z(i)^0.3*exp(-z(i)) ; The synchrotron function
F(i)=N(i)*P(i)
Endfor

Flux(k)=int_tabulated(gama,F)*4409.98*1e+23;/ 4409.98*the first fatctor is correction
tf=20 j=k-tf
```

```
if (j lt 1) then Flux2(k)=0 else Flux2(k)=Flux(k-20)
norm_factor=int_tabulated(gama,N)
Endfor

Flare=2*(Flux-Flux2)
Return
End
```

; This function finds the solution of the trascendental equation 4.13 for given γ and hence estimates the cooling length.

```
Function transcedental, gama,t ; The inputs for this function are γ and time
COMMON parameters
x=findgen(100000)*0.001
y1=(gama_max/gama_not-1.0)*exp(-x)
y2=gama_max/gama-t/tacc+x*(1-us/cs)-1
ans=min(abs(y1-y2),index)
return, sol
End
```

B IDL Program to Fit the Pulses

```
Pro Pulse_Fitting
; This program fits the light curve and reproduces it from the given center time, amplitude and width.

; Reading the data
npts=2613 ; Number of points in the file
datain=fltarr(2,npts)
readf,1,datain
close,1

; x= time and y= flux
x=datain(0,*)
y=datain(1,*)*1000.0 ; Scaling for better numbers

;Read the parameter from the parameter file
openr,2,"C: parameters.dat"
data=fltarr(4,28)
readf,2,data
close,2

center=data(1,*) ; Second column of the parameters fiel is the center location of the pulse
background=min(y) ; the minimum of the flux is taken as the background flux level
AMP=data(2,*) - background
FWHM=data(3,*) ; Fourth column is the width of the pulse
Width=FWHM/2.335*13 ; Scaling to fit the data
```

; The flare data obtained from the previous program

flare=[0.00321419 , 0.0140696 , 0.0412252 , 0.135276 , 0.320829 ,$
0.735687, 1.16632 , 1.86539 , 2.86370 , 3.91220 ,$
4.94337, 6.10291 , 7.31108 , 8.35510 , 9.36189 ,$
10.2908, 11.0439, 11.7778, 12.3548, 12.8509, $
13.2998, 13.6546, 13.9295, 14.0824, 14.1086, $
13.8645, 13.5780, 12.9947 , 12.0968 , 11.1282, $
10.1632 , 9.05835 , 7.89404 , 6.88743 , 5.91146,$
5.00740 , 4.27543 , 3.55865 , 2.99553 , 2.51124, $
2.07212 , 1.71124 , 1.41603 , 1.17464 , 0.967543, $
0.800632 , 0.659771 , 0.546742 , 0.448608 , 0.370576]

; New variable declartaion

new_x=fltarr(35,2613)
flare1=fltarr(35,2613)
Fitting=fltarr(2613)

For i= 0,35 do begin
for j=0,2612 do begin
new_x(i,j)=(x(j)-center(i))*50/width(i)+23.0 ; The offset for the center is 23.0 and 50 is the total number of points in the pulse
flare1(i,j)=interpolate(flare,new_x(i,j), cubic=-0.5,missing=0)/14.1086*AMP(i)
Endfor
Endfor

For k=0,2612 do begin
Fitting(k)=total(flare1(*,k))+min(y) ; The pusles co-adding on top of the background

```
Endfor

plot,x,y ; Plotting the light curve
oplot,x,fitting,psym=3 ; Overplotting the fitting with different symbol
print,correlate(y,flare1) ; Correlation coefficient
End
```

LIST OF REFERENCES

Angel I. R. P. &Stockman H. S., 1980. Annu. Rev. Asfron. Asfrophys. 1 8:321-61 12

Beall J. H., Snyder W. A., &Wood K . S., 1988. Proc. IAU Symp. 134, edt DE Osterbrock, JS Miller, pp. 106-7. Dordrecht: Reidel 10

Begelman, M. C., Blandford, R. D., & Rees, M. J. 1984, Rev. Mod. Phys., ApJ 314, 699 38

Begelman, M. C., & Sikora, M., ApJ 322, 650 (1987) 8

Biermann et al., 1981, ApJ, 247, L53 14

Blandford R.D., and Levinson A., ApJ 441, 79 (1995). 7, 9, 40

R. Blandford, A. Konigl, 1979, ApJ, 232,34 6

Blazejowski M., Sikora M., Moderski R., and Madejski G.M., ApJ 545, 107 (2000). 7

Bracewell R. , "The Fourier Transform and its Application", McGraw-Hill, (1965) 26

Brinkmann W, Maraschi L, Treves A, Urry CM, Warwick R, et aI. 1994. Astron. Astrophys. 288:433-47 11

de Bruyn A. G. 1988. Proc. IAU Symp. 129, edt MJ Reid, JM Moran pp. 97-98. Dordrecht:Reidel 12

Burbidge, G. R. 1959, ApJ, 129, 849 39

Celotti, A., Ghisellini, G., MNRAS 385, 283300 (2008) 46, 47

Courvoisier T., Blecha A, Bouchet P, Bratschi P, Carini M. T., et al. 1995. Ap. J. 438:108-19 12

Daubechies, I., 1992. Ten Lectures on Wavelets, SIAM Press, Philadelphia 30

Deeming, T.J.,1975, Ap& SS, 36, 137. 26

Dent W. A., 1965. Science 148:1458-60 12

Dermer C.D., and Schlickeiser R., ApJ 416, 458 (1993). 9

Dermer C.D., and Chiang J., New Astr. 3, 157 (1998). 7

Dhalla S., Webb J., Bhatta G. and Pollock J., JSAFRA, 4, 1-5, (2010) 32, 33

Downs, Webb J., & Pollock, Private Communication 15

Edelson R. A., Saken M., Pike G. F., Urry C. M., George M, et al. 1991. Ap. J. Lett. 372:L9-L12 11

Edelson R. A. 1992. Ap. J. 401:516-28 11

Efanov V. A., Moiseev I. G., Nesterov N. S., Shakhovskoy N. M. 1977. Nature 269:493-94 12

Elliot J. L. & Shapiro S. L. 1974. Ap. J. Lett. 192:L3-L6 11

Falkovich G.& Sreenivasan K.R. Lessons from hydrodynamic turbulence, 2006, Physics Today, vol. 59, no. 4, 4349 53

Farge, M. 1992, Ann. Rev. Fluid Mech., 24, 395 31

Feigelson E.D., Bradt H., McClintock J, Remillard R, Urry CM, et al. 1986. Ap. J. 302:337-51 11

Gaidos J.A. et al., Nature 383, 319 (1996). 7

George M., Warwick R. S. , Bromage G. B., 1988, MNRAS 232:793-808 11

Ghisellini G., and Maraschi L., ApJ 340, 181 (1989). 7

Ghisellini G., and Madau P., MNRAS 280, 67 (1996). 9

Ghisellini G. et al., 1997, A&A, 327, 61 14

Ghisellini, G., Tavecchio, F.,& Chiaberge, M., A&A 432, 401 (2005) 9

Giommi P, Barr P, Garilli B, Maccagni D, Pollock AMT. 1990. Ap. 1. 356:432-55 11

Gupta A., Srivastava A., & Witta, P., 2009, ApJ, 690,216. 15, 30, 33

Hartmann, R.C., Webb, J.R., Marscher, A. P., Travis, J. P., Dermer, C. D., Aller, H. D., Aller, M. F., Balonek, T. J., Bennett, K., Bloom, S.D., Fujimoto, R., Hermsen, W., Hughes, P., Jenkins, P.J., Kii, T., Kurfess, J. D., Makino, F., Mattox, J. R., von Montigny, C., Ohashi, T., Robson, I., Ryan, J., Sadun, A., Schoenfelder, V., Smith, A. G., Terasranta, H., Tornikoski, M., and Turner, M. J. L., 1996, Ap. J., 461, 698. vii, 4

Harvey G. A., Andrew B. H., MacLeod J. M., Medd W., 1972, Astrophys. Lett. 1 1 : 147-49 12

Heidt J., Wagner S. J., 1996, A&A, 305, 42 20

Holmes P. A., Brand P., Impey C. D., Williams P. M., Smith P., et al. 1984. MNRAS 21 1 :497-506 12

Hoyle F, Burbidge G. R., Sargent W., 1966. Nature 209 :7 51-53 12

Jorstad, S. G., et al. 2001, ApJS, 134, 181 39

Jorstad, S. G., et al. 2005, AJ, 130, 1418 39

Kellermann, K. I., et al. 2004, ApJ, 609, 539 39

Kerrick A. D., Akerloff C. W., Biller S. O., Buckley J. H., Cawley M. F., et al. 1995. Ap. 1. Lett. 438:L59 -62 11

Kirk J. G., Mastichiadis A. 1992. Nature, 360:135-37 11

Kirk J., D. Melrose and E. Priest , "Plasma Astrophysics", Springer-Verlag, (1994) 8, 36

Kirk J. G., Reiger F. M., & Mastichiadis A., Astron. Astrophys. 333, 452-458 (1998) 40, 46, 54

Khembhavi G. & Narlikar J. , "Quasars and Active Galactic Nuclei", Cambridge University Press (1999) 44

Kohmura Y, Makishima K, Tashiro M, Ohashi T, Urry CM. 1994. Publ. Astron. Soc. Jpn. 46: 1 3 1-38 11

Komissarov S.S., and Falle S.A.E.G., MNRAS 288, 833 (1997). 7

Konigl A, ApJ 243:700-709 1981 39

Krolik J. H., "Active Galactic Nuclei", Princton University Press, (1999) 2

Kuhr H., Pauliny-Toth I. I. K., Witzel A., Schmidt J., 1981, AJ, 86, 854 14

Lesch H, Pohl M. 1992 Astron. Astrophys. 254:29-38 11

Mannheim K., and Biermann P.L., A&A 253, L21 (1992). 9

Mannheim, K., A&A 221, 211 (1993) 10

Maraschi L, Tagliaferri G, Tanzi E. G., Treves A. 1986. Ap. J. 304:637-45 11

Marscher, A. P. 1980, ApJ, 235, 386 40

Marscher, A. P. 1983, ApJ, 264, 296 39

Marscher A.P., and Gear W.K., ApJ 298, 114 (1985). 7, 8, 36

Marscher, A. P., & Gear, W. K., ApJ 298, 114 (1985) 8, 36

Marshall H. L., Carone T. E., Fruscione A. 1993. Ap. 1. Lett. 414:L53-L56 11

Meier, D. L., Koide, S., & Uchida, Y. 2000, Science, 291, 84 39, 40

Michelson P. F., Chiang J, Fierro J. M., Lin Y. C., Nolan P, L., et al. 1994. In The Second Compton Symposium. ed. CE Fichtel, N Gehrels, JP Norris, AlP Conf. Proc. 304:602-10. New York: Am. Inst. Phys. 11

Montagni et al., 1995, ApJ, 440, 525:553 14

Montagni, F., 2006, A&A, 451,435. 15, 23

Moore, R. L., Angel, J. R. P., Duerr, R., Lebofsky, M. J., Wisniewski, W. Z., Rieke, G. H.,Axon, D. J., Bailey, J., Hough, J. M., McGraw, J. T.,1982, ApJ.260,415M 12

Moore R. L., Schmidt G. D., West S. C., 1987, Ap, 1.314:176-86 12

Nilsson K., Pursimo T., Sillanpää A., Takalo L. O., Lindfors E., 2008, A&A, 487, L29 14

Nesci R., Massaro E., Rossi C., Sclavi S., Maesano M., Montagni F., 2005, AJ, 130, 1466 14, 15

Paczynski B. 1986. Ap. J. 301 :503-16 10

Piner, B. G. 2006, in Future Directions in High Resolution Astronomy, ed. J. D. Romney & M. J. Reid, ASP Conf. Ser., 340, 55 39

Pope, Stephen B. Turbulent Flows. Cambridge University Press 2000 53

Quirrenbach, A., Witzel, A., Wagner, S., Sanchez-Pons, F., Krichbaum, T. P., Wegner, R., Anton, K., Erkens, U., Haehnelt, M., Zensus, A., & Johnston, K. (1991), ApJ. 14

Raiteri, C. M., Villata, M., Tosti, G., Nesci, R., Massaro, E., Aller, M. F., Aller, H. D., Tersranta, H., Kurtanidze, O. M., Nikolashvili, M. G., Ibrahimov, M. A., Papadakis, I. E., Krichbaum, T. P., Kraus, A., Witzel, A., Ungerechts, H., Lisenfeld, U.; Bach, U., Cim, G., Ciprini, S., Fuhrmann, L., Kimeridze, G. N., Lanteri, L., Maesano, M., Montagni, F., Nucciarelli, G., Ostorero, L., 2003, A&A, 402, 151. 15

Remillard R. A., Grossan B, Bradt H. V., Ohashi T, Hayashida K, et al. 1991 . Nature 350:589-92 11

Rybicki G. & Lightman A. , "Radiative Processes in Astrophysics", John Wiley & Sons (1979) 41

Sambruna R.M., et al., ApJ 538, 127 (2000). 7

Shimada N., and Hoshino M., ApJ 543, L67 (2000). 8

Sholomitskii G. B., 1965. Astron. Zh. 42:673-674; trans!. Sov. Astron. 9:516-17 12

Shu F., "The Physics of Astrophysics Vol I Radiation", University Science Books, (1991) 12

Sikora M., Begelman M.C., Rees M.J., ApJ 421, 153 (1994). 8, 9

Sikora, M., & Madejski, G. 2000, ApJ, 534, 109 40

Sikora, M., Blazejowski, M., Begelman, M. C., & Moderski, R., ApJ 554, 1 (2001); Erratum: ApJ 561, 1154 (2001) 8, 37

Smith, Michael D. , "Astrophysical Jets and Beams", Cambridge (2012), p. 31 53

Snyder W. A., Davidsen A. F., Wood K, Kinzer R, Smathers H, et al. 1980. Ap. I Lett. 237:L1 1- L14 11

Sokolov, A., Marscher, A. P., & McHardy, I. A., ApJ 613, 725 (2004) 8, 37

Takahashi T., et al., ApJ 543, L124 (2000). 7

Urry, C., Padovani, P, 1995, PASP, 107, 803U 2

Vaughan, S., Edelson, R., Warwick, R. S., & Uttley, P., 2003, MNRAS, 345, 1271. 32

Villata, M., Raiteri, C. M., Lanteri, L., Sobrito, G., & Cavallone, M.,1998,A&AS, 130, 305. 16

Villata, M et al., A&A(2000), 363, 108-116. 15, 23

Vlahakis, N., & Knigl, A. 2004, ApJ, 605, 656 40

von Montigny C., et al., ApJ 440, 525 (1995). 7

Wagner S. J., Witzel A, Krichbaum T. P., Wegner R, Quirrenbach A, et al. 1993. Astron. Astrophys. 271 :344-47 12

Wagner S. J., Witzel A., 1995, ARA &A, 33, 163 14

Wagner S. J. et al., 1996, AJ, 111, 2187 14

Wagner S. J., Witzel A, Heidt J, Krichbaum T. P., Quirrenbach A, et a!. 1995c. Astron. J. 11

Webb J. R., Smith A. G., Leacock R. J., Fitzgibbons G.L., Gombola P. P., Shepherd D. W., 1988. Astron. J. 95:374-97 12

Webb, J.R., 2007, AAS, 210.0202W 14

Webb, J. R., 2010, BAAS, 21642011W. 14

Wehrle A.E., et al., ApJ 497, 178 (1998). 7

Witzel A, Quirrenbach A. 1993. In Propagation Effects in Space VLBl, ed. N Kardashev, L Gurvits, pp. 33-44. Ithaca, NY: Natl. Astron. Ionosp. Cent. 11

Wu, J., Peng, B., Zhou, X., Ma, J, Jiang, Z., Chen, J. (2005), AJ., 129, 1818. 15

Wu J., Zhou X., Ma J., Wu Z., Jiang Z., Chen J., 2007, AJ, 133, 1599 14

Wu, J., Zhou, X., Ma, J., Wu, Z., Jiang, Z., & Chen, J., (2007), AJ, 133, 1599. 15

Zhang X., Zheng Y. G., Zhang H. J., Liu Y.,Wen Y. B.,WangW., 2008, AJ,136, 1846 14

http://www.bu.edu/blazars/research.html

http://heasarc.gsfc.nasa.gov/docs/cgro/images/epo/gallery/agns/index.html viii, 36, 37

http://heasarc.gsfc.nasa.gov/docs/cgro/images/epo/gallery/agns/index.html 2 6

VITA

Gopal P. Bhatta

RESEARCH INTERESTS

My main interests are the multi-frequency study of AGNs, Physical processes around black holes, radiations from relativistic jets and shock waves in plasma..

EDUCATION

2000	M.Sc., Physics Tribhuvan University, Kathmandu, Nepal
2007-2011	Graduate Assistant Florida International University Miami, Florida
2012	Graduate Assistant Florida International University Miami, Florida
2012	Dissertation Year Fellowship Award Florida International University

Honors and Awards

Second Prize Award, Graduate Student Research Competition, Department of Physics, Florida International University, 2012

Second Prize Award, Graduate Scholarly Forum Research Competition, Florida International University, 2012

Dissertation Year Fellowship, Florida International University, 2012

Best Astronomy Teaching Assistant, Florida International University, 2011

Graduate student speaker award in the Miami physics conference 2008, Lago Mar Resort, Fort Lauderdale, Florida

Hilmor Louis Astronomy Scholarship, for 'Someone in Love with Stars', 2007

Publications

The Nature of Microvariability in Blazar 0716+71, AAS Meeting #215, #434.11; Bulletin of the American Astronomical Society, Vol. 42, p.376.

Multi-frequency monitoring of the blazar 0716+714 during the GASP-WEBT-AGILE campaign of 2007, A&A 481, L79L82 (2008)

The 72-hour WEBT Observation of Microvariability in Blazar 0716+714 (Submitted)

Conference Presentations

WEBT Observations of Blazar 0716+714, AAS 2012, # 219, # 209.02D

A Model for Microvariability in Blazars, AAS 2011, # 218, # 327.04

Microvariability in Blazars, AAS 2010, #216,#420.11 Microvariability in Blazars, Miami physics conference 2008, Lago Mar Resort, Fort Lauderdale, Florida